On eddy transport in the ocean. Part II: The advection tensor

Michael Haigh [a,*], Luolin Sun [a], James C. McWilliams [b], Pavel Berloff [a,c]

[a] *Department of Mathematics, Imperial College London, London, United Kingdom*
[b] *Department of Atmospheric and Oceanic Sciences, University of California Los Angeles, CA, 90095, United States of America*
[c] *Institute of Numerical Mathematics of the Russian Academy of Sciences, 119333 Moscow, Russia*

ARTICLE INFO

ABSTRACT

This study considers the isopycnal eddy transport of mass and passive tracers in eddy-resolving double-gyre quasigeostrophic oceanic circulation. Here we focus on advective transport, whereas a companion paper focuses on eddy-induced diffusive tracer transport. To work towards parameterising eddy tracer transport we quantify the eddy tracer flux using a transport tensor with eddies defined using a spatial filter, which leads to results distinct from those obtained via a temporal Reynolds eddy decomposition. The advection tensor is the antisymmetric part of the transport tensor, and is so named since the associated tracer transport can be expressed as advection of the large-scale tracer field by a rotational eddy-induced velocity (EIV) $\boldsymbol{u}_*^c$ with streamfunction A. The EIV $\boldsymbol{u}_*^c$ is fastest (~ 1 m s^{-1}) where eddy activity is strongest, e.g., in the upper layer, near the eastward jet and western boundary current. Our results suggest that a stochastic closure for the eddy transport would be most suitable since A exhibits a probabilistic distribution when conditioned on, for example, the large-scale relative vorticity. Consistent with closures in ocean circulation models, we quantify eddy mass (isopycnal layer thickness) fluxes as eddy-induced advection by the thickness EIV $\boldsymbol{u}_*^h$. The divergent part of $\boldsymbol{u}_*^h$ – the only part relevant for mass transport in the quasigeostrophic limit – tends to be oriented down the thickness gradient suggesting it quantifies some baroclinic eddy effects similar to those parameterised by the Gent & McWilliams (GM90) EIV. Although $\boldsymbol{u}_*^h$ has some qualitative similarities to $\boldsymbol{u}_*^c$, our results suggest that eddy-induced tracer advection is driven by more than just the thickness-determined EIV and, in turn, more than just the GM90 EIV.

1. Introduction

The transport of passive tracers by oceanic mesoscale eddies remains an inadequately understood aspect of oceanic circulation. Given that mesoscale eddies are often unresolved in general circulations models, a good understanding of eddy transport is required in order improve parameterisations of their effects. A typical method for parameterising eddy tracer transport is via a transport tensor $\boldsymbol{K}$ that acts upon the large-scale tracer gradient. There are numerous methods for diagnosing $\boldsymbol{K}$. In this study we take a direct approach by simulating passive tracers in a high-resolution double-gyre ocean model, and from the eddy tracer fluxes we diagnose $\boldsymbol{K}$. The transport tensor $\boldsymbol{K}$ can be decomposed into its symmetric and antisymmetric components which encompass diffusive and advective effects, respectively. Part I of this study, Haigh et al. (2021) (hereafter HSMB21) focuses on the symmetric diffusion tensor, whereas here we focus on the antisymmetric advection tensor, $\boldsymbol{A}$. The advection tensor is so named since its associated skew flux is equivalent to advection of the large-scale tracer field by an *eddy-induced velocity* (EIV), $\boldsymbol{u}_*^c$ (Griffies, 1998).

Eddy mass (isopycnal thickness) transport is accounted for in coarse-grid ocean models by including an eddy-induced advection by the thickness EIV, $\boldsymbol{u}_*^h$. In most ocean models this EIV is parameterised by the Gent and McWilliams (1990) (hereafter GM90) closure. Because any dissolved materials must move if the mass does, analysis of the thickness EIV is pertinent to tracer transport. With regard to isopycnal layer thickness, the GM90 parameterisation mimics the potential energy-releasing of effects of baroclinic eddies by flattening isopycnal surfaces. The key parameter of this closure is the 'thickness diffusivity', on which much research has focused (e.g., Visbeck et al. (1997), Killworth (1997)), but this term has caused confusion (Gent, 2011) since the GM90 scheme is best interpreted as an extra advection by an EIV (Gent et al., 1995). The same EIV is used to advect the large-scale tracer field which, combined with isopycnal diffusion, parameterises missing eddy effects on passive tracers in non-eddy-resolving ocean models. Griffies (1998) reformulated the GM90 parameterisation into its skew flux form using an antisymmetric matrix and combined it with the Redi diffusion tensor (Redi, 1982) to represent isopycnal advective and diffusive eddy tracer transport in *z*-coordinate models.

---

* Corresponding author.
  E-mail address: m.haigh15@imperial.ac.uk (M. Haigh).

We will consider the relationship between the EIVs $\boldsymbol{u}_*^c$ and $\boldsymbol{u}_*^h$ as diagnosed in our ocean model. See Eden and Greatbatch (2009) who relate the difference between these EIVs to the angles between the gradients of large-scale tracers and isopycnals. The interpretation of the EIVs (and the diffusive tracer transport) depends on the method for classifying diffusive and advective transport. Some studies (e.g., Andrews and McIntyre, 1978; Eden, 2010; Eden et al., 2007) define all along(across)-gradient tracer transport to be diffusive (advective), whereas other studies (e.g., Plumb and Mahlman, 1987; Bachman and Fox-Kemper, 2013; Bachman et al., 2015, 2020), including this one, employ tensors which permit diffusive fluxes to have a component across the tracer gradient. In all cases the transport coefficients depend on eddy fluxes which need to be parameterised.

The diffusive part of eddy tracer transport has also been studied extensively and was the focus of the companion study HSMB21. HSMB21 outlines two model design choices that we use in the present study. The first is the use of a spatial filter (Nadiga, 2008; Fox-Kemper and Menemenlis, 2008; Lu et al., 2016; Bachman et al., 2017a; Stanley et al., 2020) to separate the large- and small-scale (eddy) fields, as opposed to the more common Reynolds decomposition. By using a spatial filter we obtain large- and small-scale flow/tracer components that have full spatio-temporal dependence, in contrast to the Reynolds decomposition which imposes that the large-scale fields are constant in either time or one spatial coordinate (unless it is an ensemble mean). We deem this unsuitable for studies which work towards parameterisations of missing eddy effects in coarse-resolution ocean models. By using a spatial filter we are able to relate the local (in space and time) eddy tracer fluxes to the local large-scale tracer gradient via a transport tensor with full spatio-temporal dependence. In addition, the spatial filter method is becoming more suitable than the temporal Reynolds decomposition as eddy-permitting ocean models are becoming more common. This is because the validity of the temporal Reynolds decomposition relies on a distinct time scale separation between the mean and eddy components, which is lost as models become eddy-permitting (Nadiga, 2008). Our focus is on spatial filter eddies, but we will make comparisons with results obtained for 'Reynolds eddies'. Although out of the scope of this study, an alternative to the spatial filter method is the dynamical decomposition method (Berloff et al., 2021) in which a coarse-grid simulation is used to separate the large-scale and eddy components of an eddy-resolving simulation. The second method design choice regards the treatment of the eddy tracer flux. Since one of our targets is a physical interpretation of the eddy tracer flux, we argue it is important to remove its dynamically inert rotational component. This is especially important given that the rotational component dominates the divergent component by two orders of magnitude (Marshall and Shutts, 1981; Haigh et al., 2020).

This study is organised as follows. In Section 2 we define the quasigeostrophic ocean model used for simulating double-gyre, mid-latitude oceanic circulation. We then outline the method for obtaining the transport tensor from the eddy tracer fluxes. In Section 3 we briefly present the transport tensor. Then in Section 4.1 we consider the advection tensor and the associated tracer EIV. In Section 4.2 we introduce the parameterisation approach for eddy mass fluxes. We compare the EIVs for passive tracer and mass transport in Section 4.3. Since the ultimate goal is parameterisation of the missing eddy effects, in Section 4.4 we discuss the relationship between the EIVs and features of the large-scale flow. In Section 5 we consider results for eddies defined using a temporal Reynolds decomposition. Lastly, in Section 6 we conclude and discuss our results.

2. The model

2.1. The dynamical model

The ocean model used in this study is outlined in HSMB21 and Haigh et al. (2020), so here we will be brief. We use a wind-driven, three-layer quasigeostrophic (QG) model set up in a square basin to simulate double-gyre, mid-latitude flow. In layer k, the QG potential vorticity (PV) equation is

$$\frac{\partial q_k}{\partial t} + J(\psi_k, q_k) + \beta \frac{\partial \psi_k}{\partial x} = \nu \nabla^4 \psi_k - \delta_{3k}\gamma \nabla^2 \psi_k + \frac{\delta_{1k}}{\rho_1 H_1} W, \quad (1)$$

where q_k is the QG PV anomaly and ψ_k is the streamfunction. Also, J is the Jacobian operator; $\beta = 2 \times 10^{-11}$ m^{-1} s^{-1} is the planetary vorticity gradient; $\nu = 20$ m^2 s^{-1} is the Laplacian eddy viscosity; $\gamma = 4 \times 10^{-8}$ s^{-1} is the linear bottom friction coefficient; $\rho_1 = 10^3$ kg m^{-3} is the upper-layer density; δ_{ij} denotes the Kronecker delta. W represents asymmetric tilted wind forcing as defined in HSMB21 and Haigh et al. (2020).

The upper ($k = 1$), middle ($k = 2$) and lower ($k = 3$) layers have static thicknesses of $H_1 = 250$ m, $H_2 = 750$ m and $H_3 = 3$ km, respectively, and the basin has side length $L = 3840$ km. The PV and streamfunctions in each layer are related via

$$q_1 = \nabla^2 \psi_1 + s_1(\psi_2 - \psi_1), \quad (2)$$

$$q_2 = \nabla^2 \psi_2 + s_{21}(\psi_1 - \psi_2) + s_{22}(\psi_3 - \psi_2), \quad (3)$$

$$q_3 = \nabla^2 \psi_3 + s_3(\psi_2 - \psi_3). \quad (4)$$

The stratification parameters, s_1, s_{21}, s_{22} and s_3, are selected such that the first and second Rossby deformation radii are 40 km and 20.6 km, respectively. We use partial-slip conditions on the lateral boundaries, with a boundary sub-layer lengthscale of 120 km (Berloff and McWilliams, 1999). The QG PV equations are simulated using the CABARET scheme (Karabasov et al., 2009) with the domain uniformly discretised on a 1025^2 grid. This corresponds to a grid resolution of 3.75 km, sufficient to resolve mesoscale eddy activity.

In this study we will consider eddy mass fluxes, in which case it is necessary to define the isopycnal thickness of each layer. These thicknesses are

$$h_1 = H_1 + \frac{f_0}{g_1'}(\psi_1 - \psi_2) + \frac{f_0}{g}\psi_1, \quad (5)$$

$$h_2 = H_2 + \frac{f_0}{g_1'}(\psi_2 - \psi_1) + \frac{f_0}{g_2'}(\psi_2 - \psi_3), \quad (6)$$

$$h_3 = H_3 + \frac{f_0}{g_2'}(\psi_3 - \psi_2), \quad (7)$$

where $f_0 = 0.83 \times 10^{-4}$ s^{-1} is the mid-latitude Coriolis parameter, $g = 9.81$ m s^{-2} is the gravitational acceleration and $g_1' \approx 0.018$ m s^{-2} and $g_2' \approx 0.013$ m s^{-2} are the reduced gravities between the first and second, and the second and third layers, respectively.

2.2. The tracer model

We are interested in the eddy transport of passive tracers C whose layer-wise evolution is governed by the advection–diffusion equation,

$$\frac{\partial C}{\partial t} + \nabla \cdot (\boldsymbol{u}C) = \nu \nabla^2 C + F, \quad (8)$$

where we have dropped the layer subscript k for brevity. Here $\boldsymbol{u} = \hat{\boldsymbol{z}} \times \nabla \psi$ is the isopycnal velocity field, where $\hat{\boldsymbol{z}}$ denotes the vertical unit vector, and F represents external sources/sinks which will be defined shortly.

To model eddy tracer transport it is necessary to decompose the flow and tracer fields into large and small scales. We use a spatial filter (Nadiga, 2008; Fox-Kemper and Menemenlis, 2008; Lu et al., 2016; Bachman et al., 2017a; Stanley et al., 2020) to extract the large-scale component of a field. That is, for a snapshot of a discrete field $\phi_{i,j}$, where i, j are the zonal and meridional indices of the grid point, the local large-scale component is defined as the average over all grid points spanned by the square filter centred on grid point i, j. Thus, the large-scale component of $\phi_{i,j}$ is

$$\overline{\phi}_{ij} = \frac{1}{w^2} \sum_{m=i-l}^{i+l} \sum_{n=j-l}^{j+l} \phi_{mn}, \quad (9)$$
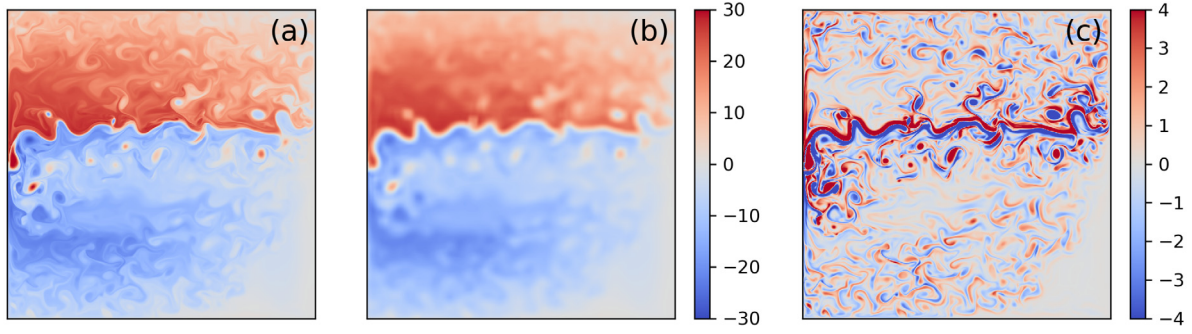
Fig. 1. (a) The upper-layer PV anomaly q, (b) its large-scale part $\overline{q}$ and (c) its small-scale part q'. The PV here is dimensionless. Panels (a) and (b) share a colorbar. In this figure, and all following figures showing fields in a given layer, the x-axis represents longitude and the y-axis represents latitude.

where w is the filter width and $l = (w-1)/2$. We take $w = 31$ which corresponds to a physical filter width of 112.5 km, approximately three times the first deformation radius. Given the large-scale field $\overline{\phi}_{ij}$, the small-scale field is $\phi'_{ij} = \phi_{ij} - \overline{\phi}_{ij}$. Herein we will drop the i, j notation.

Using the above spatial filter, the evolution equation for the large-scale tracer field is

$$\frac{\partial \overline{C}}{\partial t} + \nabla \cdot (\overline{\boldsymbol{u}} \overline{C}) + \nabla \cdot \boldsymbol{f} = \nu \nabla^2 \overline{C} + \overline{F}, \tag{10}$$

where the divergence of the *eddy tracer flux* $\boldsymbol{f}$ is

$$\nabla \cdot \boldsymbol{f} = \overline{\nabla \cdot (\boldsymbol{u}C)} - \nabla \cdot (\overline{\boldsymbol{u}} \overline{C}). \tag{11}$$

The eddy tracer flux $\boldsymbol{f}$ represents the portion of the tracer transport that would hypothetically be unresolved in a coarse-resolution ocean model, but nonetheless influences the evolution of the large-scale tracer field.

The form of the eddy tracer flux as in (11) is most common in large-eddy simulation studies (Lilly, 1967; Leonard, 1975; Fox-Kemper and Menemenlis, 2008)). An alternate, but equivalent, definition for $\boldsymbol{f}$ can be obtained by directly decomposing all terms in the full tracer budget and comparing the result with the filtered tracer budget. Doing this leads to

$$\nabla \cdot \boldsymbol{f} = \nabla \cdot \boldsymbol{g} + \frac{\partial C'}{\partial t} - \nu \nabla^2 C' - F', \tag{12}$$

where $\boldsymbol{g} = \overline{\boldsymbol{u}} C' + \boldsymbol{u}' \overline{C} + \boldsymbol{u}' C'$ is the *unfiltered eddy tracer flux*. Haigh et al. (2020), Kamenkovich et al. (2021) and Sun et al. (2021) focus on the transport tensor representation of the $\boldsymbol{g}$ flux only and propose parameterising the linear eddy terms separately. However, eddy balances exist between $\nabla \cdot \boldsymbol{g}$ and the linear eddy terms, meaning that analysis of $\boldsymbol{g}$ is not necessarily pertinent to the large-scale tracer evolution. For this reason we will primarily focus on $\boldsymbol{f}$, but in section 4.3 we will use the $\boldsymbol{g}$ flux for the purpose of comparison with eddy mass transport.

The filter does not commute with the divergence operator near the boundaries which prevents us from obtaining an explicit global expression for $\boldsymbol{f}$. This does not pose an issue since we are interested in just the divergent part of the eddy tracer flux, $\boldsymbol{f}_{\text{div}}$, as the rotational part is dynamically inert. In addition, the rotational part dominates the divergent part by two orders of magnitude (Marshall and Shutts, 1981) so its inclusion in our analysis would inhibit a proper physical interpretation of the eddy tracer flux. To obtain $\boldsymbol{f}_{\text{div}}$ we use a Helmholtz decomposition (Lau and Wallace, 1979):

$$\boldsymbol{f} = \nabla \phi + \hat{\boldsymbol{z}} \times \nabla \chi + \mathcal{H}, \tag{13}$$

where ϕ is a divergent potential, χ is a streamfunction and $\mathcal{H}$ is a non-divergent, irrotational gauge term (Maddison et al., 2015). We invert the Poisson equation $\nabla^2 \phi = \nabla \cdot \boldsymbol{f}$ for the divergent potential ϕ using the physically motivated boundary condition $\phi = 0$ (Maddison et al., 2015). The divergent eddy tracer flux is then $\boldsymbol{f}_{\text{div}} = \nabla \phi$.

We now define the tracer source/sink as

$$F = r(C_0 - \overline{C}). \tag{14}$$

This represents relaxation of the large-scale tracer field back to its initial condition, C_0, at a relaxation rate r. We will motivate this choice for F in the next section. We use tracers that have linear initial conditions of the form

$$C_0 = \frac{ax + by + c}{\sqrt{a^2 + b^2}}, \tag{15}$$

where a, b and c are constants. In addition to being the initial condition, (15) represents the profile towards which the large-scale tracer fields are restored.

2.3. The filtered QG solution

The QG solution is spun up from rest until statistical equilibrium and is run for another year with data saved daily, on which our analysis is based. The upper-layer flow contains a fast eastward jet which is characterised by a sharp meridional PV gradient, and is flanked by broad recirculation gyres. In the middle layer the jet's signature is a weak eastward flow, with a more homogenised PV field. In the lower layer, the instantaneous flow is populated mostly by eddies/Rossby waves. After time averaging it is clear that alternating latent jets exist at most latitudes (Chen et al., 2016). In Fig. 1 we show snapshots of (a) the upper-layer PV anomaly, (b) its large-scale part and (c) its small-scale part. As observed by Berloff (2018), the eddy PV field q' features a ribbon of opposite-signed PV that straddles the jet core. This dipole pattern augments the relatively weak cross-jet PV gradient in the large-scale field $\overline{q}$. Elsewhere, the eddy PV field is populated by filaments, fronts and vortices. Large vortices can have a clear signal in $\overline{q}$ but filaments and fronts (other than the jet) are more difficult to observe.

3. The transport tensor

Working towards parameterising the divergent eddy tracer flux, $\boldsymbol{f}_{\text{div}}$, here we introduce the transport tensor. Using the flux-gradient relation we relate $\boldsymbol{f}_{\text{div}}$ to the large-scale tracer gradient $\nabla \overline{C}$ via the transport tensor $\boldsymbol{K}$:

$$\boldsymbol{f}_{\text{div}} = -\boldsymbol{K} \nabla \overline{C}. \tag{16}$$

Here $\boldsymbol{K}(x, y, t)$ is a 2×2 tensor with full spatio-temporal dependence. For just one tracer system (16) is underdetermined which we overcome by simulating two tracers, C_1 and C_2, which have divergent fluxes $\boldsymbol{f}_1 = (f_1^{(u)}, f_1^{(v)})$ and $\boldsymbol{f}_2 = (f_2^{(u)}, f_2^{(v)})$. Inverting (16) for these two tracers gives

$$\boldsymbol{K} \equiv \begin{pmatrix} K_{11} & K_{12} \\ K_{21} & K_{22} \end{pmatrix} = \frac{1}{d} \begin{pmatrix} f_1^{(u)} & f_2^{(u)} \\ f_1^{(v)} & f_2^{(v)} \end{pmatrix} \begin{pmatrix} -\overline{C}_{2,y} & \overline{C}_{2,x} \\ \overline{C}_{1,y} & -\overline{C}_{1,x} \end{pmatrix}, \tag{17}$$

where $d = \overline{C}_{1,x} \overline{C}_{2,y} - \overline{C}_{1,y} \overline{C}_{2,x}$ is the determinant of the matrix of large-scale tracer gradients. To avoid the singularity at $d = 0$, the tracers are initialised with misaligned large-scale gradients. The relaxation forcing F defined in (14) is motivated by the need to maintain this

misalignment throughout the simulation. We use a relaxation timescale of 5 days, but results are not greatly dependent on our choice. In particular, the qualitative behaviour of the transport tensor does not change under reasonable variations in the relaxation rate, but the amplitude of K can change (Haigh et al., 2020).

In this study we use a single pair of tracers to determine K as a function of space and time. While the diagnosed K is non-unique – meaning that in general K depends on the choice of tracer pair (Kamenkovich et al., 2021; Sun et al., 2021) – it is independent of our choices of a, b and c in the linear restoring fields (15), i.e., K is the same for all tracer pairs with linear restoring fields. Two factors contribute to this being true. First, because we remove the rotational part of the eddy tracer flux, the constant c in the large-scale tracer restoring fields (15) does not contribute to K. Second, the linearity of the flux-gradient relation (16) and the tracer evolution equation (8) mean that K is the same for any pairs of tracers that are linear combinations of one another (i.e., of the form $AC_1 + BC_2$, for $A, B \in \mathbb{R}$). We also simulated tracers with wave-like large-scale restoring fields and found that the resulting transport tensor, while not exactly the same, retains the same qualitative behaviour. A further discussion of the non-uniqueness of K is given in Section 6. Plots and a deeper discussion of K are given in HSMB21.

We separate the transport tensor into its symmetric (S) and anti-symmetric (A) components,

$$S = \frac{1}{2}\left(K + K^T\right) \quad \text{and} \quad A = \frac{1}{2}\left(K - K^T\right). \tag{18}$$

We refer to the symmetric component S as the *diffusion tensor* since its associated fluxes are diffusive, with tracer mixing properties dependent on its eigenvalues. The companion paper HSMB21 focused on S and showed that the eigenvalues are robustly of opposite sign, such that the diffusive flux is interpreted as driving tracer filamentation. In this study we focus on the *advection tensor* A. Only the off-diagonal elements of K, namely K_{12} and K_{21}, contribute to A which is uniquely defined by $A = -A_{12} = A_{21}$. Elements K_{12} and K_{21} also contribute to the diffusion tensor via the element S_{12}. The elements A_{12} and S_{12} are of the same amplitude in each layer. The tracer tendency due to A is comparable in amplitude to the diffusive flux divergence associated with S.

4. Advective transport

Advective transport is parameterised by including an extra advection by an *eddy-induced velocity* (EIV) in the necessary evolution equation. In this section we consider advective eddy transport of both passive tracers and isopycnal layer thickness (mass). Using the framework of Gent and McWilliams (1990) and Gent et al. (1995) advective eddy transport of mass and tracers is parameterised in general circulation models (CGMs) using the same EIV, with the remainder of the eddy tracer transport parameterised as a diffusive process. Because the same thickness-determined EIV parameterises both advective eddy tracer and mass transport, and because tracers must be transported whenever mass is, diagnoses of eddy mass transport are pertinent to eddy tracer transport. Comparison of tracer-determined and thickness-determined EIVs will illuminate to what extent a thickness-determined EIV can parameterise the entirety of the advective eddy tracer transport, a key assumption of Gent and McWilliams (1990) and Gent et al. (1995).

4.1. The advection tensor

4.1.1. The formulation

We refer to A as the advection tensor because the associated tracer forcing can be expressed as advection of the large-scale tracer field (Plumb and Mahlman, 1987; Gent et al., 1995; Visbeck et al., 1997; Griffies, 1998) by the tracer eddy-induced velocity (EIV),

$$\boldsymbol{u}_*^c = \hat{\boldsymbol{z}} \times \nabla A = \left(-\frac{\partial}{\partial y}A, \frac{\partial}{\partial x}A\right), \tag{19}$$

where $A = -A_{12} = A_{21}$ is the streamfunction for the EIV $\boldsymbol{u}_*^c$. The advective flux is

$$\boldsymbol{f}_{\text{adv}} = \boldsymbol{u}_*^c \overline{C}. \tag{20}$$

Since $\boldsymbol{u}_*^c$ is non-divergent (rotational) the associated tracer tendency is $\boldsymbol{u}_*^c \cdot \nabla \overline{C}$. The same tracer tendency is obtained for the skew flux (Griffies, 1998),

$$\boldsymbol{f}_{\text{skew}} = \nabla \overline{C} \times A\hat{\boldsymbol{z}}. \tag{21}$$

The components of the skew flux are qualitatively similar to A since in our case the large-scale tracer fields are roughly linear. The skew flux and the advective flux are related via

$$\boldsymbol{f}_{\text{adv}} = \boldsymbol{f}_{\text{skew}} + \hat{\boldsymbol{z}} \times \nabla\left(A\overline{C}\right), \tag{22}$$

which shows that they differ by a non-divergent vector field. The difference between $\boldsymbol{f}_{\text{adv}}$ and $\boldsymbol{f}_{\text{skew}}$ is simply a spatial transport with no spatially integrated effect.

Although the skew and advective fluxes have the same divergence, they have entirely different magnitudes and orientations. Moreover, the advective flux has a rotational part that dominates the divergent part by two orders of magnitude, as was the case with the original eddy tracer flux. Despite the parameterised flux due to K being irrotational (by design), the skew flux does have a rotational part, but this is comparable in amplitude to its divergent part. This rotational component is equal and opposite to the rotational component of the diffusive flux and can be interpreted as a correction necessary to render the fluxes due to S and A diffusive and skew, respectively. Some authors prefer the skew flux formulation since it can be easily implemented by extending a diffusion tensor closure in ocean models, and because $\boldsymbol{f}_{\text{skew}}$ is likely to be a less noisy field (Griffies, 1998) than $\boldsymbol{f}_{\text{adv}}$ which contains an extra derivative of A.

4.1.2. Results

The time-mean A, denoted $\langle A \rangle$, and its standard deviation in each layer are shown in Fig. 2. In each layer A is typically largest near the jet or the western boundary, both locations with strong eddy activity. In the upper layer we observe a cross-jet dipole pattern in $\langle A \rangle$ caused by $\langle K_{21} \rangle$. That is, sufficiently far from the western boundary current we have positive/negative $\langle A \rangle$ to the south/north of the jet core. This pattern leads to tracer flux convergence/divergence on the jet core when the zonal large-scale tracer gradient is negative/positive, and this augments a similar contribution by the diffusive flux convergence. Similar, albeit weaker, cross-jet patterns exist in the two layers below. These patterns in A are associated with eastward EIVs in the jet that augment zonal advection by the large-scale flow. Expectedly, the standard deviations are largest where the eddy activity is strongest.

In Fig. 3 we show three snapshots (100-day interval between snapshots) of A from each layer. The cross-jet sign change in $\langle A \rangle$ leads to notable time-mean eastward EIVs in each layer, but the presence of this is much less obvious at a given instant. In the lower layer, coherent patterns are less prevalent in the instantaneous fields, whereas in the two layers above we can identify features in common between A and $\langle A \rangle$. In the upper layer the EIV speed $u_*^c = |\boldsymbol{u}_*^c|$ can be as large as 1 m s^{-1} in the jet, comparable to the speed of the jet itself, and is typically on the order of 0.01 m s^{-1} away from the jet. In the middle and lower layers, typical speeds are a few millimetres per second, with largest speeds in the jet region. Overall, it is clear that $\boldsymbol{u}_*^c$ has a very complicated spatial dependence, and thus its effects on the tracer field are by no means homogeneous. We will discuss the tracer EIV $\boldsymbol{u}_*^c$ further in Section 4.3.
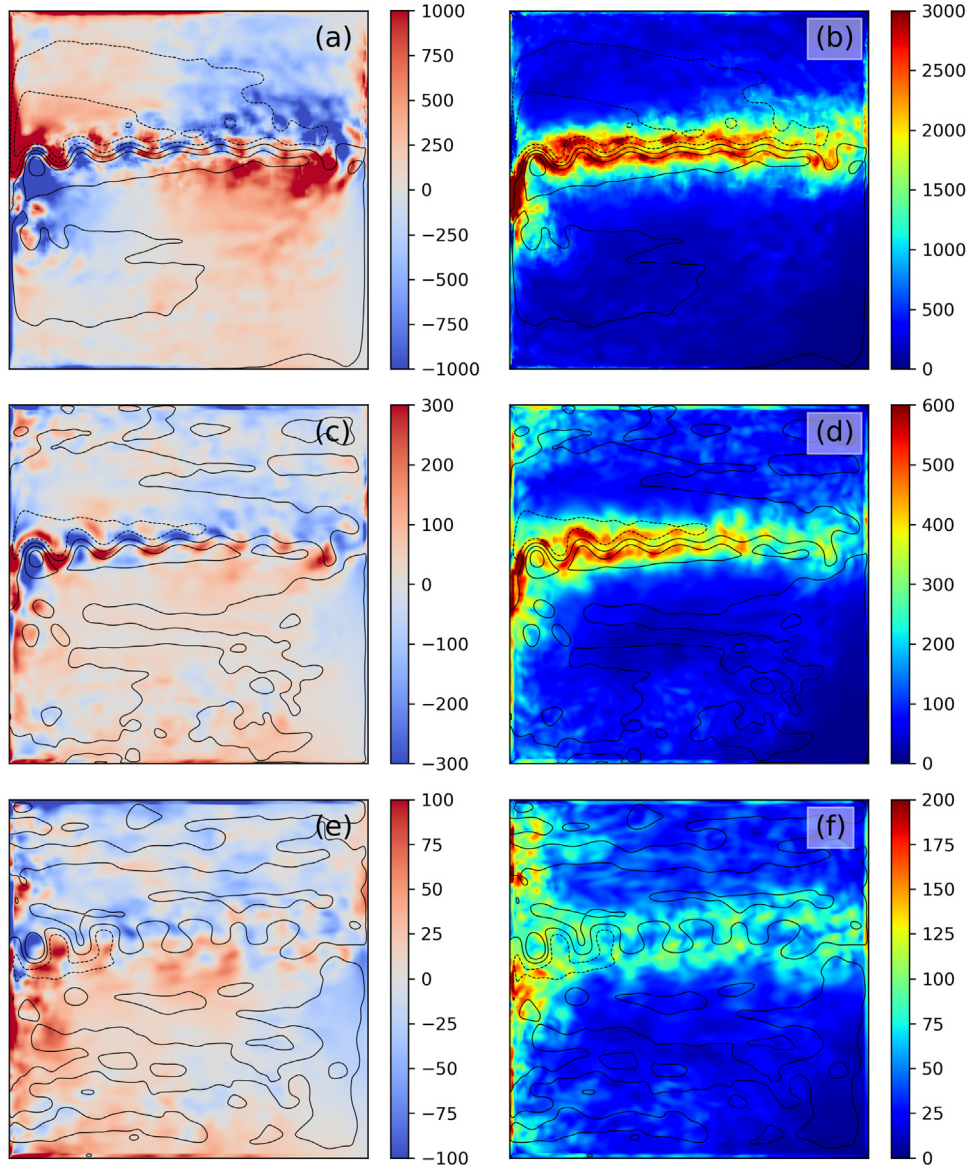
Fig. 2. The time-mean (a, c, e) and standard deviation (b, d, f) of the off-diagonal advection tensor component and tracer EIV streamfunction $A = -A_{12} = A_{21}$. These are for the upper (a, b), middle (c, d) and lower (e, f) layers. Units are m^2 s^{-1} in all panels. Contours represent the time-mean large-scale streamfunction.

4.2. Eddy mass transport

Eddy transport of isopycnal layer thickness or mass, h, is parameterised in GCMs by including an extra advection term, based on the formulation of Gent and McWilliams (1990), hereafter GM90. In this formulation, GM90 and Gent et al. (1995) showed that tracers and mass can be expressed as being advected by the same EIV which is dependent on the eddy thickness flux. This thickness EIV parameterises all eddy effects for thickness, but not for tracers, with the remainder of the eddy effects assumed to be diffusive (Redi, 1982). See Appendix A in which we derive an alternative tracer equation demonstrating how the tracer can be explicitly expressed as being advected by the thickness EIV for our QG model. The closure for the thickness EIV proposed by GM90, which is now a broadly implemented feature of GCMs, parameterises the potential energy-releasing effects of baroclinic eddies. Since GM90 dozens of studies (e.g., Danabasoglu et al., 1994; McDougall and McIntosh, 1996, 2001; Smith and Gent, 2004; Gent, 2011; Grooms and Kleiber, 2019; Bachman, 2019) have sought to implement, test or improve this closure. Given that the GM90 framework is a broadly implemented and successful feature of GCMs,

in this study we will diagnose EIVs consistent with the framework. We do this by considering the thickness-determined EIV $\boldsymbol{u}_*^h$ derived directly from eddy mass fluxes of our QG model. Then, with the context that a thickness-determined EIV parameterises advective eddy tracer transport in GCMs, we compare $\boldsymbol{u}_*^h$ with $\boldsymbol{u}_*^c$. This comparison will shed light on the capability of thickness-determined EIVs to parameterise the entirety of the advective eddy tracer transport, a key assumption of GM90.

4.2.1. The formulation

In each layer the QG thickness equation is

$$\frac{\partial h}{\partial t} + \nabla \cdot \left(\boldsymbol{u} h + \boldsymbol{u}_a H \right) = 0, \tag{23}$$

where $\boldsymbol{u}_a$ is the ageostrophic velocity. Filtering the above equation gives

$$\frac{\partial \overline{h}}{\partial t} + \nabla \cdot \left(\overline{\boldsymbol{u}} \overline{h} \right) + \nabla \cdot \boldsymbol{f}^h + H \overline{\nabla \cdot \boldsymbol{u}_a} = 0, \tag{24}$$

where, by analogy with the large-scale tracer equation (10), the eddy mass flux is defined via its divergence

$$\nabla \cdot \boldsymbol{f}^h = \overline{\nabla \cdot (\boldsymbol{u} h)} - \nabla \cdot (\overline{\boldsymbol{u}} \overline{h}). \tag{25}$$
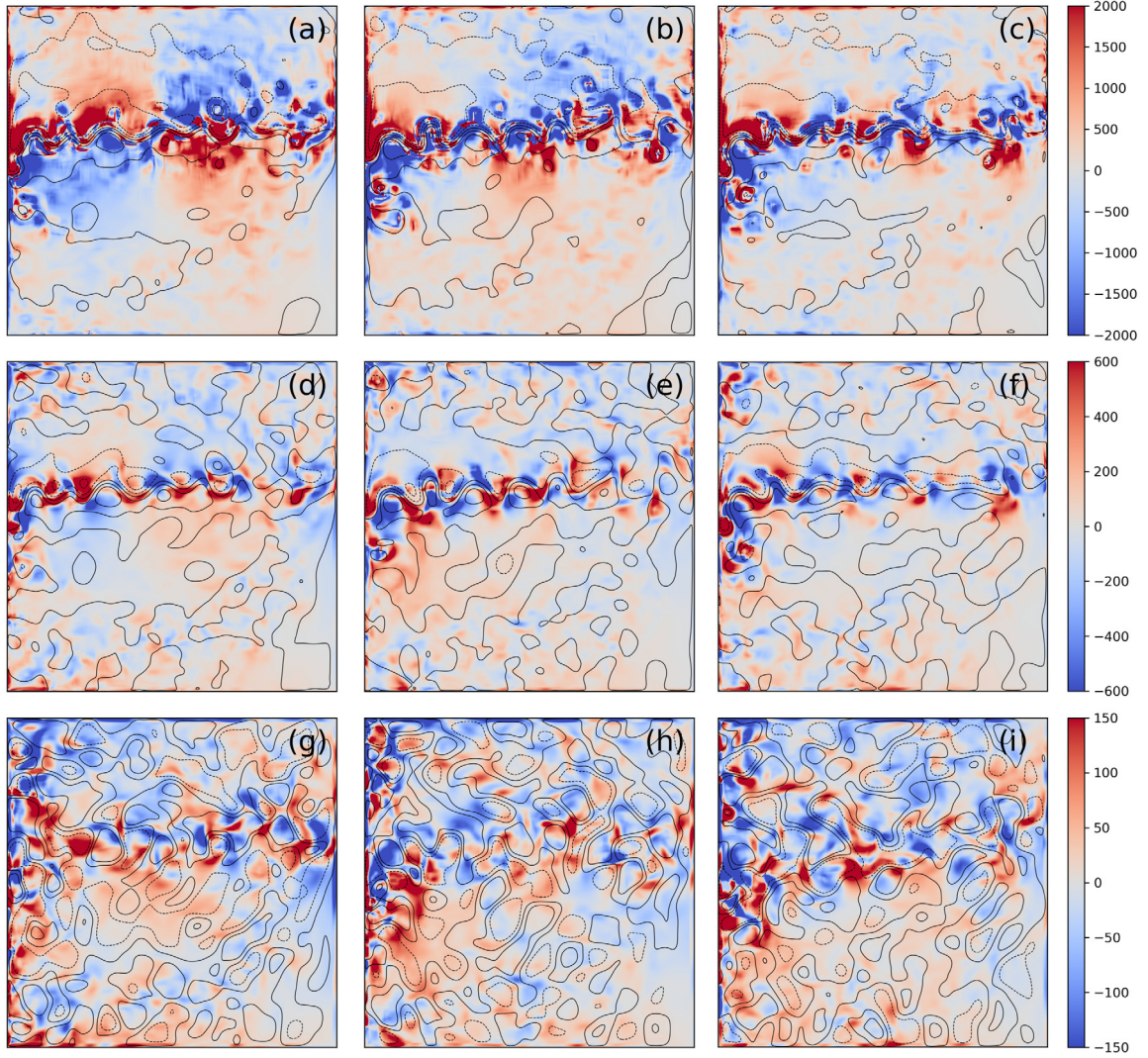
Fig. 3. Snapshots of the advection tensor component $A(= -A_{12} = A_{21})$ in the upper (a, b, c), middle (d, e, f) and lower (g, h, i) layers. The snapshots in panels (a, d, g) are taken at an arbitrary time. The snapshots in panels (b, e, h) are taken 100 days later and those in panels (c, f, i) are taken 200 days later. We show multiple snapshots to emphasise the temporal dependence. Units are m² s⁻¹. Contours represent snapshots of the large-scale streamfunction.

In the QG limit the lateral eddy thickness fluxes are formally of negligible order (Treguier et al., 1997), but as QG models are successfully applied outside of their formal limits of applicability (Mundt et al., 1997; Zurita-Gotor and Vallis, 2009; Shevchenko and Berloff, 2015), we diagnose these fluxes to be of leading order. Since our results have intended implications for more complete (primitive equation) ocean models, and since we work within the GM90 framework, these thickness fluxes are a focus of this study. It is possible to extend the analysis to include the extra ageostrophic velocity contribution, but we are only interested in the action of geostrophic eddies because only these enter into the passive tracer budget.

It is technically possible to apply an eddy diffusion closure to thickness, in the same manner as for passive tracers, but unlike passive tracers isopycnal thickness is not materially conserved and so does not satisfy the assumptions necessary for eddy diffusion theory to apply. Moreover, the eddy mass flux in GCMs is parameterised as eddy-induced advection by an EIV, and there is little motivation to move outside of such a well-established framework. Within this framework we relate the eddy mass flux $\boldsymbol{f}_h$ to the thickness EIV $\boldsymbol{u}_*^h$ using the equations

$$\boldsymbol{u}_*^h = \frac{\boldsymbol{f}^h}{\overline{h}} \quad \text{and} \quad \nabla \cdot \boldsymbol{f}^h = \nabla \cdot \left(\boldsymbol{u}_*^h \overline{h} \right). \tag{26}$$

Eqs. (26) apply to eddy mass transport in primitive equation models and can be simplified slightly in the QG limit where formally[1] $\overline{h} \approx H$ so that

$$\boldsymbol{u}_*^h \approx \frac{\boldsymbol{f}^h}{H} \quad \text{and} \quad \nabla \cdot \left(\boldsymbol{u}_*^h \overline{h} \right) \approx H \nabla \cdot \boldsymbol{u}_*^h. \tag{27}$$

Only at grid points that lie at least one half of the filter's width away from the boundaries, where the filter operator commutes with the divergence operator and where we may write $\boldsymbol{f}^h = \overline{\boldsymbol{u}h} - \overline{\boldsymbol{u}}\overline{h}$, can $\boldsymbol{u}_*^h$ be diagnosed.

We show in Appendix A that the large-scale tracer in our model can be expressed as being advected by the thickness EIV $\boldsymbol{u}_*^h$, as in the original GM90 formulation. The remaining eddy effects are assumed by GM90 to be diffusive. In our model all eddy effects on the tracer are already accounted for by $\boldsymbol{K}$, but whether or not the eddy effects

---

[1] It is possible for QG models to be successfully applied outside of their formal limits of applicability, in which case H is not a good approximation to $\overline{h}$. For example, in the upper layer of our simulations $\overline{h}_1$ can deviate more than 100 m away from $H_1 = 250$ m. This may demotivate assuming that $\overline{h} \approx H$, but we stress making this assumption is not necessary, but rather motivated by formal QG theory. Removing this assumption is also necessary to extend the formulation to the primitive equations, in which case the focus should be shifted to the *eddy-induced transport*, $T_* = \boldsymbol{u}_*^h \overline{h}$.

on tracers quantified by $\boldsymbol{u}_*^h$ are precisely accounted for by $\boldsymbol{u}_*^c$ is not yet known. Differences between $\boldsymbol{u}_*^h$ and $\boldsymbol{u}_*^c$ would imply that tracers should be advected by more than just $\boldsymbol{u}_*^h$ in the GM90 formulation. That $\boldsymbol{u}_*^h$ has both rotational and divergent parts and that $\boldsymbol{u}_*^c$ is purely rotational is an early indication that $\boldsymbol{u}_*^h$ and $\boldsymbol{u}_*^c$ are distinct objects.

We will compare the full $\boldsymbol{u}_*^h$ with $\boldsymbol{u}_*^c$, but we can only do this at grid points at least one half of the filter's width away from the boundaries where the filter commutes with the derivative. Because only the divergent part of $\boldsymbol{u}_*^h$ influences the mass evolution in the QG limit, and because $\boldsymbol{u}_*^c$ is purely rotational whereas $\boldsymbol{u}_*^h$ has both rotational and divergent parts, extracting divergent and rotational parts from $\boldsymbol{u}_*^h$ will be useful. The divergent part of the thickness EIV is obtained by inverting the Poisson equation

$$\nabla^2 \boldsymbol{\Phi} = \frac{1}{H} \nabla \cdot \boldsymbol{f}^h \qquad (28)$$

with boundary condition $\boldsymbol{\Phi} = 0$ (Maddison et al., 2015), and then setting

$$\boldsymbol{u}_{*d}^h = \nabla \boldsymbol{\Phi}. \qquad (29)$$

Because we do not have an explicit global expression for $\boldsymbol{f}^h$ and $\boldsymbol{u}_*^h$, we cannot implement a complete Helmholtz decomposition and cannot obtain a unique rotational EIV that defines the entire rotational part of $\boldsymbol{u}_*^h$. As a compromise we express a portion of $\nabla \cdot \boldsymbol{f}^h$ as a flux divergence, for which there are multiple options. Decomposing the terms in the total mass budget yields an alternate expression for $\nabla \cdot \boldsymbol{f}^h$:

$$\nabla \cdot \boldsymbol{f}^h = \nabla \cdot \boldsymbol{g}^h + \frac{\partial h'}{\partial t} + H \left(\nabla \cdot \boldsymbol{u}_a \right)'. \qquad (30)$$

Here $\boldsymbol{g}^h = \overline{\boldsymbol{u}} h' + \boldsymbol{u}' \overline{h} + \boldsymbol{u}' h'$ is the *unfiltered eddy mass flux* for which we can calculate an associated rotational EIV $\boldsymbol{u}_{*r}^h$. This rotational thickness EIV is

$$\boldsymbol{u}_{*r}^h = \hat{\boldsymbol{z}} \times \nabla \boldsymbol{\Psi} \quad \text{where} \quad \nabla^2 \boldsymbol{\Psi} = \frac{1}{H} \hat{\boldsymbol{z}} \cdot \left(\nabla \times \boldsymbol{g}^h \right) \qquad (31)$$

is the Poisson equation for the streamfunction $\boldsymbol{\Psi}$, inverted with boundary condition $\boldsymbol{\Psi} = 0$. The outcome is a rotational thickness EIV defined using a portion $\boldsymbol{g}^h$ of the full eddy mass flux $\boldsymbol{f}^h$. We refer to $\boldsymbol{u}_{*r}^h$ as the rotational thickness EIV, but we stress that it is not the entirety of the rotational part of $\boldsymbol{u}_*^h$. Other definitions for rotational parts of $\boldsymbol{u}_*^h$ are possible, but none can lead to a complete Helmholtz decomposition.

This decomposition approach for defining $\nabla \cdot \boldsymbol{f}^h$ and $\boldsymbol{g}^h$ as in (30) is motivated by the analogous eddy tracer flux formulation as in (12). Just as $\nabla \cdot \boldsymbol{f}^h$ is contributed to by $\nabla \cdot \boldsymbol{g}^h$, the eddy tracer flux divergence $\nabla \cdot \boldsymbol{f}$ is contributed to by $\nabla \cdot \boldsymbol{g}$, where $\boldsymbol{g} = \overline{\boldsymbol{u}} C' + \boldsymbol{u}' \overline{C} + \boldsymbol{u}' C'$. For the eddy tracer flux contribution $\boldsymbol{g}$ we denote the EIV and associated streamfunction as $\boldsymbol{u}_*^g$ and A^g, respectively. We use the eddy flux contributions $\boldsymbol{g}$ and $\boldsymbol{g}^h$ and the corresponding EIVs $\boldsymbol{u}_*^g$ and $\boldsymbol{u}_{*r}^h$ to enable comparison of two purely rotational EIVs derived from counterpart terms in the tracer and mass budgets. This approach is also useful because recent studies (Haigh et al., 2020; Kamenkovich et al., 2021; Sun et al., 2021) propose parameterising the unfiltered eddy tracer flux $\boldsymbol{g}$ separately from the linear eddy terms, since $\boldsymbol{g}$ is the only actual eddy flux term in the large-scale tracer budget. Comparing $(\boldsymbol{u}_*^c, \boldsymbol{u}_*^g)$ with $(\boldsymbol{u}_*^h, \boldsymbol{u}_{*r}^h)$ will show how well the thickness EIVs account for the advective eddy tracer transport.

4.2.2. Results

The time mean and standard deviation of the divergent potential $\boldsymbol{\Phi}$ in each layer is shown in Fig. 4, and a sequence of snapshots of $\boldsymbol{\Phi}$ is shown in Fig. 5. A prevailing spatial pattern in $\boldsymbol{\Phi}$ – present in all layers and clearer after time-averaging – is a zonal oscillation in the jet region. This implies that the zonal component of $\boldsymbol{u}_{*d}^h$ alternates in sign and converges/diverges where $\boldsymbol{\Phi}$ is locally maximised/minimised. In all three layers these convergences/divergences are centred on northward-/southward-oriented sections of the large-scale flow meanders. By the QG-approximated eddy mass forcing parameterisation in

(27), this convergence/divergence of $\boldsymbol{u}_{*d}^h$ is equivalent to flux convergence/divergence of thickness. However, these areas are also where the gradients of the thickness anomaly are least negligible, and can cause leading-order cross-jet mass fluxes that contribute to the eastward jet maintenance (Berloff, 2005). The EIV $\boldsymbol{u}_{*d}^h$ is fastest in the upper layer ($\sim 10^{-3}$ m s^{-1}) and slowest in the lower layer ($\sim 10^{-4}$ m s^{-1}), so that it is typically two orders of magnitude slower than the tracer EIV $\boldsymbol{u}_*^c$, implying that any effects on tracer transport are negligible.

In Fig. 6 we show the time-mean and standard deviation of $\boldsymbol{\Psi}$, the streamfunction for the rotational thickness EIV contribution. Snapshots of $\boldsymbol{\Psi}$ are very similar to the mean and similar to the eddy streamfunction, so we opt to not show these for brevity. The streamfunction $\boldsymbol{\Psi}$ is an order of magnitude larger than the potential $\boldsymbol{\Phi}$ and this scale difference is magnified in the rotational ($\boldsymbol{u}_{*r}^h$) and divergent EIVs ($\boldsymbol{u}_{*d}^h$), the former being typically two orders of magnitude larger than the latter. In the lower layer the mean thickness $H_3 = 3$ km is large relative to the thickness anomalies, so that the contribution from the eddy flux component $\boldsymbol{u}' \overline{h} \approx \boldsymbol{u}' H$ dominates the other two components. Since $\boldsymbol{u}' H$ is purely rotational it does not influence the thickness dynamics. Specifically, in the lower layer we have

$$\boldsymbol{\Psi} \approx \psi' \quad \text{and} \quad \boldsymbol{u}_{*r}^h \approx \boldsymbol{u}', \qquad (32)$$

where ψ' and $\boldsymbol{u}'$ are the eddy streamfunction and velocity, respectively. In the middle layer, where $H_2 = 750$ m, the above remains a reasonable approximation, whereas in the upper layer, where $H_1 = 250$ m, the approximation does not apply. Nearer the surface the large-scale-eddy $\overline{\boldsymbol{u}} h'$ and eddy–eddy $\boldsymbol{u}' h'$ fluxes become more significant, and these contain important velocity-thickness correlations that represent baroclinic instability. These correlations are not necessarily restricted to the $\boldsymbol{u}' h'$ flux, but will be mostly present in $\boldsymbol{u}' h'$ because this component represent interactions on the smallest scales.

In Fig. 7 we show the time-mean $\boldsymbol{u}_*^h$ in each layer. These plots omit grid points within half the filter's width of any boundary, since in these boundary regions $\boldsymbol{u}_*^h$ cannot be diagnosed. The thickness EIV $\boldsymbol{u}_*^h$ is on the order of 0.01 m s^{-1} near the jet in upper layer and is on the order of 0.001 m s^{-1} elsewhere in the upper layer. In the middle and lower layers $\boldsymbol{u}_*^h$ is between one and two orders of magnitude slower than in the upper layer. The standard deviation of $\boldsymbol{u}_*^h$ (not shown) has spatial structure similar to the standard deviation of $\boldsymbol{\Psi}$. In the upper layer, on the northern flank of the jet $\boldsymbol{u}_*^h$ exhibits time-mean flow in the direction of the jet while on the southern flank $\boldsymbol{u}_*^h$ exhibits time-mean flow in the direction opposite to the jet. We observe similar time-mean behaviour in the middle and lower layers, but with the direction opposite to the upper layer. Persistent qualitative patterns such as these are most clear in the jet region of each layer, and these are distinct from the qualitative features of the tracer EIV $\boldsymbol{u}_*^c$ which tends to be an along-jet or counter-jet velocity on the jet core, rather than the flanks. In the next section we will compare $\boldsymbol{u}_*^h$ and $\boldsymbol{u}_*^c$ directly, to better quantify differences between them across the rest of the domain.

4.3. A comparison of thickness and tracer EIVs

In this section we compare the tracer and thickness EIVs. While $\boldsymbol{u}_*^c$ is purely rotational, the thickness EIV $\boldsymbol{u}_*^h$ has both divergent and rotational parts, implying that they are distinct objects, but the extent of their differences is yet to be quantified. A comparison between the tracer and thickness EIVs and a comparison of their rotational contributions $\boldsymbol{u}_*^g$ and $\boldsymbol{u}_{*r}^h$, will shed light on the capability of thickness EIVs to account for advective eddy tracer transport in oceanic mesoscale eddy parameterisations.

4.3.1. Scalings

Here we present and compare typical magnitudes of the EIVs and their contributions. Table 1 presents root mean square (rms) values for $(A, \boldsymbol{\Psi}, \boldsymbol{\Phi})$ and $(\boldsymbol{u}_*^c, \boldsymbol{u}_{*r}^h, \boldsymbol{u}_{*d}^h, \boldsymbol{u}_*^h)$ in each layer. (For the EIVs, we compute the rms values of the EIV speeds.) The tracer EIV $\boldsymbol{u}_*^c$ has rms values of
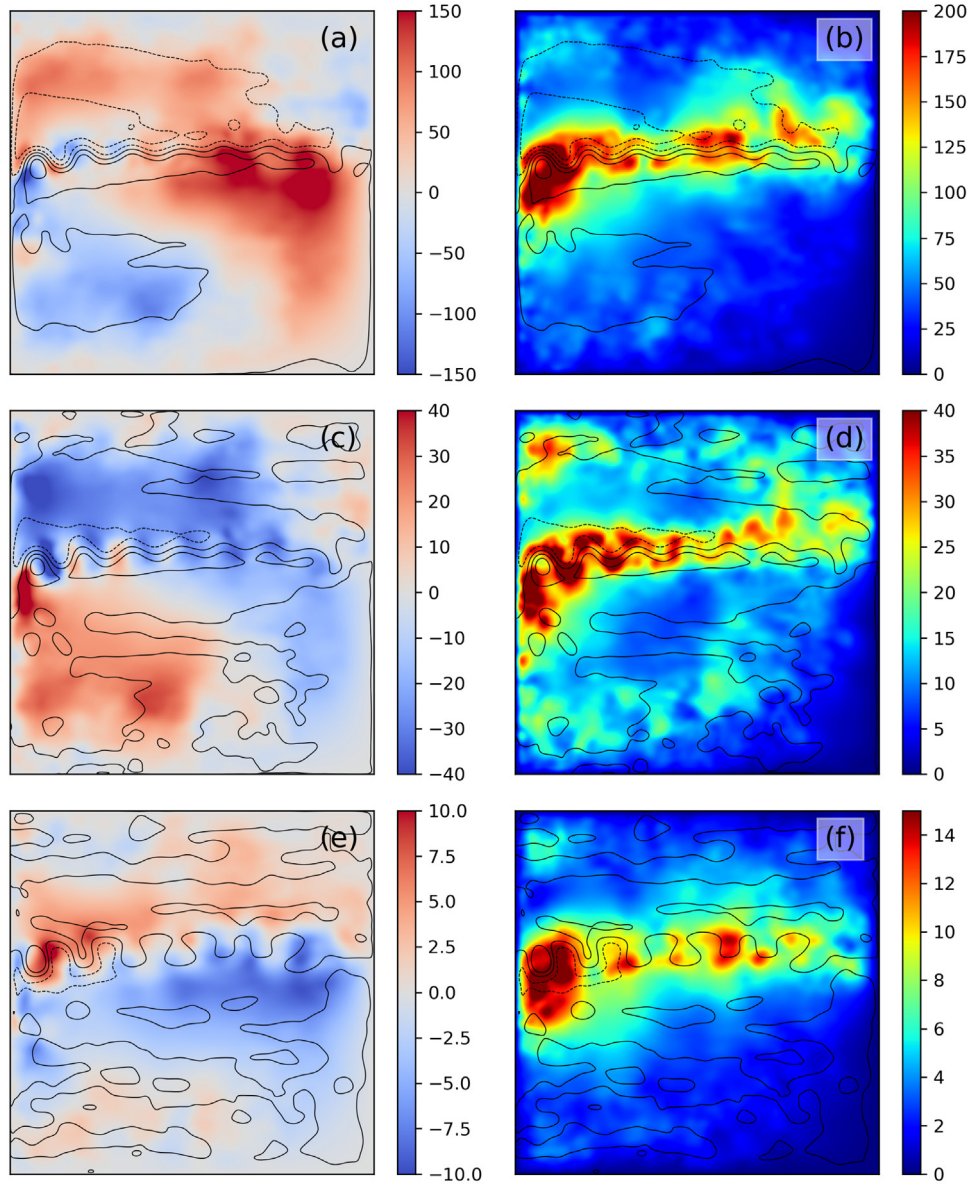
Fig. 4. The time-mean (a, c, e) and standard deviation (b, d, f) of Φ, the potential for the divergent thickness EIV. These are for the upper (a, b), middle (c, d) and lower (e, f) layers. Units are m^2 s^{-1} in all panels. Contours represent the time-mean large-scale streamfunction.

a few centimetres per second in the upper layer and a few millimetres per second in the layers below. The rotational EIV contribution $\boldsymbol{u}_{*r}^h$ is on the order of 0.01 m s^{-1} in all layers. The divergent EIV $\boldsymbol{u}_{*d}^h$ has rms values two orders of magnitude smaller than $\boldsymbol{u}_{*r}^h$. In each layer the full thickness EIV $\boldsymbol{u}_*^h$ has rms values roughly between one sixth and one third the size of $\boldsymbol{u}_*^c$, dependent on the layer. Note, the EIVs and contributions other than $\boldsymbol{u}_*^h$ have rms values enhanced by large values in the western boundary current, which do not contribute to $\boldsymbol{u}_*^h$. The notable differences in the magnitudes of $\boldsymbol{u}_*^c$ and $\boldsymbol{u}_*^h$ is more evidence that they are distinct objects and that they do not account for the same advective eddy tracer transport.

We can use scaling arguments to explain the EIV amplitudes. First we obtain a scaling for $\boldsymbol{u}_*^c$ and begin by recalling that the eddy tracer flux divergence is

$$\nabla \cdot \boldsymbol{f}_{\text{div}} = \overline{\boldsymbol{u} \cdot \nabla C} - \overline{\boldsymbol{u}} \cdot \nabla \overline{C}. \tag{33}$$

The form of the parameterisation adopted in this study is

$$\nabla \cdot \boldsymbol{f}_{\text{div}} = -\nabla \cdot \left(S \nabla \overline{C} \right) + \boldsymbol{u}_*^c \cdot \nabla \overline{C} = \nabla \cdot \boldsymbol{f}_{\text{diff}} + \nabla \cdot \boldsymbol{f}_{\text{adv}}. \tag{34}$$

Table 1

Root mean square values of streamfunctions, potentials and corresponding EIVs in all layers. For the EIVs the rms values are the root mean squares of the EIV speeds. Averages are evaluated over one year and over all grid points. We also give rms values for $\boldsymbol{u}_*^h$, but these are computed only over grid points at least one half of the filter's width away from the boundaries. Units for the streamfunctions (A, Ψ) and potential (Φ) are m^2 s^{-1}. Units for the EIVs are m s^{-1}. All values are rounded to two significant figures. For reference the root mean square eddy velocities in upper, middle and lower layers are 0.076, 0.023 and 0.012 m s^{-1}, respectively.

	A	Ψ	Φ	$\boldsymbol{u}_*^c$	$\boldsymbol{u}_{*r}^h$	$\boldsymbol{u}_{*d}^h$	$\boldsymbol{u}_*^h$
Layer 1	1000	2100	94	0.080	0.075	0.00076	0.014
Layer 2	190	860	23	0.0060	0.024	0.00021	0.0012
Layer 3	61	510	6.1	0.0017	0.013	0.000043	0.00057

The advective ($\nabla \cdot \boldsymbol{f}_{\text{adv}}$) and diffusive ($\nabla \cdot \boldsymbol{f}_{\text{diff}}$) flux divergences are of the same amplitude, and all terms on the right-hand side of (33), including each of their contributors, contribute to $\nabla \cdot \boldsymbol{f}_{\text{adv}}$ and $\nabla \cdot \boldsymbol{f}_{\text{diff}}$ in roughly equal measure. So, we can use any term on the right-hand side of (33) for a scale prediction for $\boldsymbol{u}_*^c$. However, the scale prediction will be an overestimate when the terms in (33) have
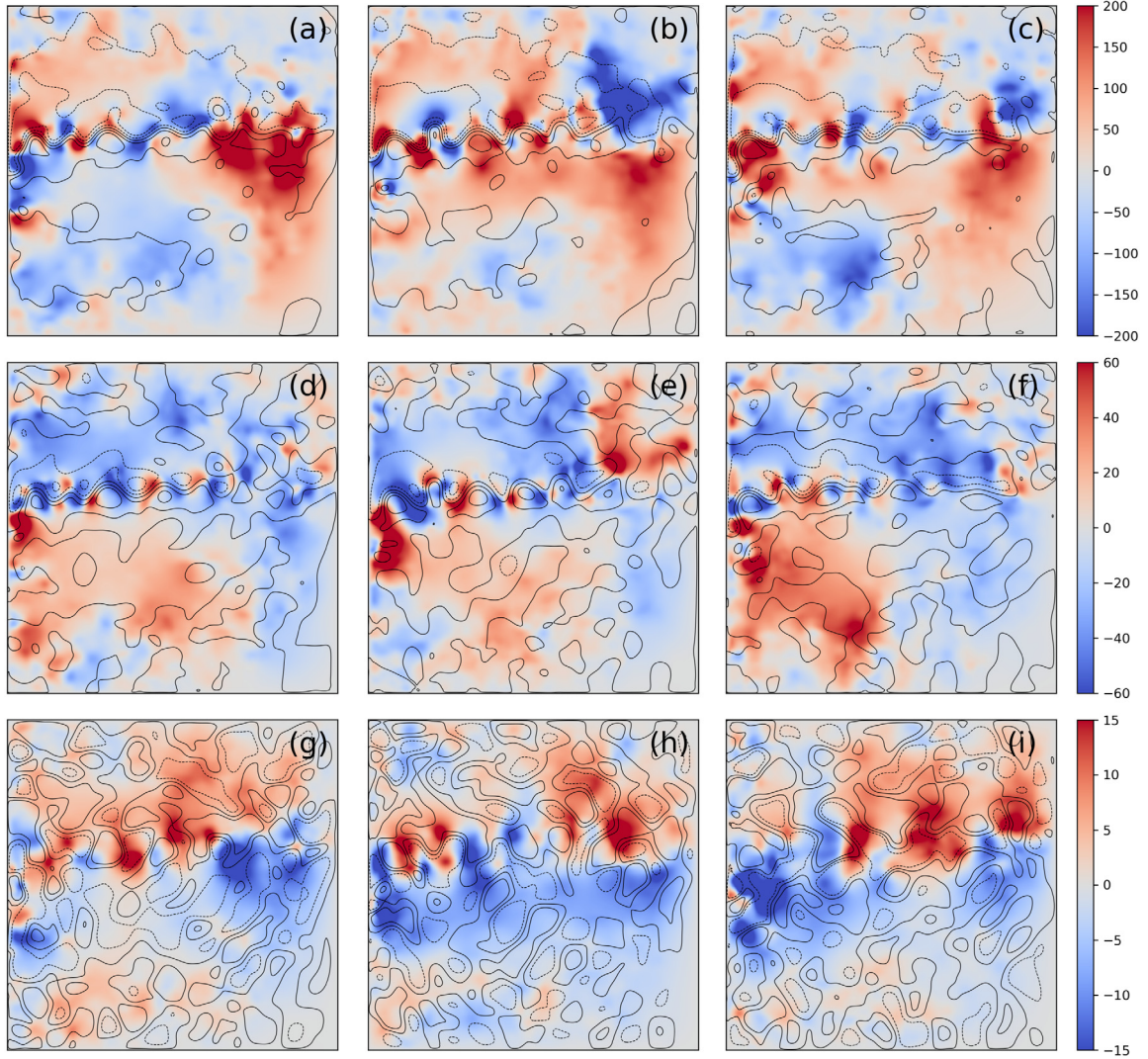
Fig. 5. Snapshots of the divergent potential Φ in the upper (a, b, c), middle (d, e, f) and lower (g, h, i) layers. The snapshots in panels (a, d, g) are taken at an arbitrary time. The snapshots in panels (b, e, h) are 100 days later and those in panels (c, f, i) are taken 200 days later. Units are m^2 s^{-1}. Contours represent snapshots of the large-scale streamfunction.

significant cancellations, which is most common in the lower layer. With this in mind, our approach leads us to predict that $u_* \sim u, \overline{u}, u'$. For reference in the upper layer the rms velocity, large-scale velocity and eddy velocity values are $u_{rms} = 0.20$, $\overline{u}_{rms} = 0.15$ and $u'_{rms} = 0.077$ m s^{-1}, respectively. These are comparable to the upper-layer rms of u_*^c. In the lower layer the velocity rms values are $u_{rms} = 0.058$, $\overline{u}_{rms} = 0.049$ and $u'_{rms} = 0.013$ m s^{-1}, but the rms of u_*^c is an order of magnitude smaller due to cancellations in the eddy tracer flux divergence.

The formal QG limit $|h'/\overline{h}| \ll 1$ suggests that the thickness EIVs may be negligible relative to the tracer EIV. However, since we use a spatial filter scale separation, the rotational EIV u_{*r}^h is contributed to by the rotational Leonard flux $u'H$, which implies that $u_{*r}^h \sim u'$. In all layers this scaling prediction is accurate. This is a reasonable scaling prediction for u_*^h in the upper layer, but in the layers below significant cancellations between g and the linear eddy terms in (30) lead to u_*^h being notably smaller than in magnitude than u'. On the divergent thickness EIV u_{*d}^h, although it is two orders of magnitude smaller than the tracer EIV u_*^c (and u_{*r}^h), this is not due to the formal QG limit $|h'/\overline{h}| \ll 1$ because in practice we often have $|h'/\overline{h}| \sim 1$. Instead, u_{*d}^h is typically two orders of magnitude smaller than the rotational EIVs because of the more general QG property that divergent velocities are order Rossby number (Ro) relative to rotational ones. The implied scaling for u_{*d}^h is $Ro\,u'$, which for a typical oceanic Rossby number of

0.01, predicts rms values in agreement with those in Table 1. That $|u_{*d}^h| \ll |u_*^c|$ implies that the transport of mass by u_{*d}^h has negligible effects in the tracer budget. Although negligible in the tracer budget, u_{*d}^h is not negligible in the QG dynamics in which baroclinic instability processes are successfully simulated (Shevchenko and Berloff, 2015).

4.3.2. Direct comparisons of EIVs

Histograms of the angles between u_*^c and u_*^h are shown for each layer in Fig. 8. These are accumulated over one year of data and over all grid points at least one half of the filter's width from the boundary, where u_*^h can be diagnosed. The EIVs u_*^c and u_*^h do not exhibit a strong tendency to be oriented in the same direction and are instead weakly related to one another. The upper layer is where the EIVs are most likely to be oriented in the same direction, but here they are equally likely to be oriented in opposite directions.

We also compare u_*^g and u_{*r}^h, along with their streamfunctions, A^g and Ψ. Both u_*^g and u_{*r}^h are derived from unfiltered eddy fluxes, $g = \overline{u}C' + u'\overline{C} + u'C'$ for passive tracers and $g^h = \overline{u}h' + u'\overline{h} + u'h'$ for thickness. The EIV u_*^g is only part of the full tracer EIV and u_{*r}^h is only part of the thickness EIV, and does not represent the entire rotational part of the thickness EIV. We compare (A^g, u_*^g) and (Ψ, u_{*r}^h) to augment comparison of u_*^c and u_*^h because u_*^c and u_{*r}^h are both rotational and because recent studies (Haigh et al., 2020; Kamenkovich et al., 2021;
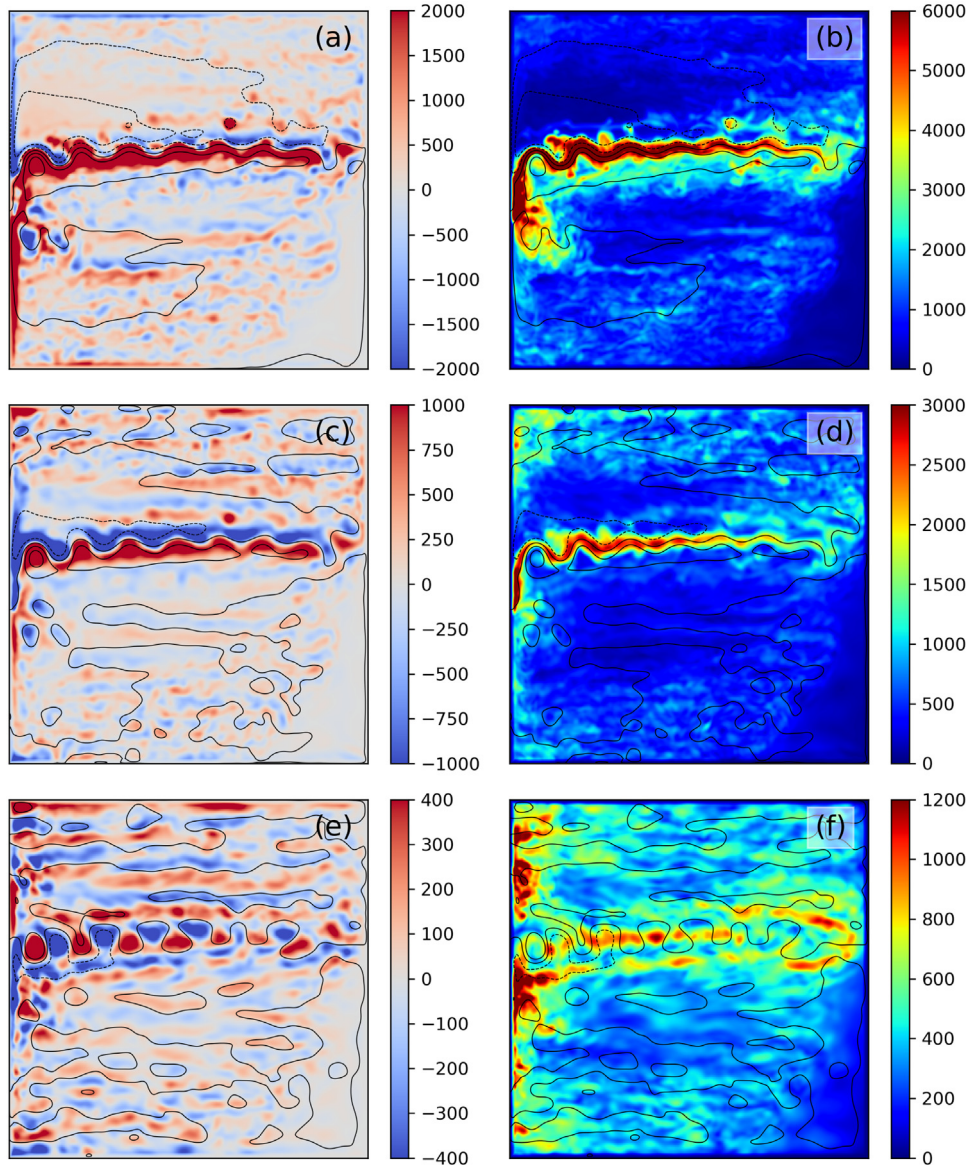
Fig. 6. The time-mean (a, c, e) and standard deviation (b, d, f) of Ψ, the streamfunction for the rotational thickness EIV. These are for the upper (a, b), middle (c, d) and lower (e, f) layers. Units are m^2 s^{-1} in all panels. Contours represent the time-mean large-scale streamfunction.

Sun et al., 2021) have proposed parameterising the g flux separately from the linear eddy terms in (12).

We present 2D histograms of A^g and Ψ in each layer in Fig. 9, along with histograms of the angle between $\boldsymbol{u}_*^g$ and $\boldsymbol{u}_{*r}^h$. There is a strong positive correlation between A^g and Ψ in the lower layer, but Ψ is approximately twice A^g. That is, we have $\Psi \approx 2A^g \approx \psi'$, where ψ' is the eddy streamfunction. In Appendix B we present a simple analytical model that explains this approximate relationship. The EIVs $\boldsymbol{u}_*^g$ and $\boldsymbol{u}_{*r}^h$ are most often oriented in the same direction. Similar, but slightly weaker, relationships between A^g and Ψ and their EIVs exist in the middle layer. In the upper layer these relationships are still visible, but are weaker than in the layers below. Comparing with the relative orientations of $\boldsymbol{u}_*^c$ and $\boldsymbol{u}_*^h$ as shown in Fig. 8, these results also show that inclusion of the linear eddy terms in (12) for the eddy tracer flux and (30) for the eddy mass flux weakens the relationship between the tracer- and thickness-determined EIVs.

From this direct comparison of $(\boldsymbol{u}_*^c, \boldsymbol{u}_*^g)$ with $(\boldsymbol{u}_*^h, \boldsymbol{u}_{*r}^h)$ we conclude that the advective eddy-induced tracer advection cannot be determined by the mass analysis. The rotational EIV contributions $\boldsymbol{u}_*^g$ and $\boldsymbol{u}_{*r}^h$ are more strongly related than the full EIVs $\boldsymbol{u}_*^c$ and $\boldsymbol{u}_*^h$, but significant differences still exist between $\boldsymbol{u}_*^g$ and $\boldsymbol{u}_{*r}^h$.

4.3.3. On differences between tracer-determined and thickness-determined EIVs

It is clear that the tracer EIV $\boldsymbol{u}_*^c$ and the thickness EIV $\boldsymbol{u}_*^h$ are distinct velocities since the former is purely rotational whereas the latter has both rotational and divergent parts. It is also the case these do not exhibit any notable tendency to be oriented in the same direction or to have the same magnitude. The rotational EIV contributions $\boldsymbol{u}_*^g$ and $\boldsymbol{u}_{*r}^h$, which are derived from the counterpart unfiltered eddy fluxes in the tracer and mass budgets, are also distinct velocity fields. In our model all eddy effects on the tracer are accounted for by the transport tensor $\boldsymbol{K}$, with the advective portion of this transport quantified by the tracer EIV $\boldsymbol{u}_*^c$, but we have shown that this eddy tracer advection cannot be determined from mass analysis. In the GM90 formulation, and as is shown in Appendix A, the thickness EIV advects passive tracers, and it was assumed by GM90 that the remainder of the eddy effects are diffusive. That our thickness and tracer EIVs are distinct does not contradict the notion that the thickness EIV should advect passive tracers in GCMs, but it does contradict the assumption of GM90 that the remainder of the eddy tracer transport (the right-hand side of equation (2) in GM90) is diffusive. The difference $\boldsymbol{u}_*^c - \boldsymbol{u}_*^h$ is an incremental EIV
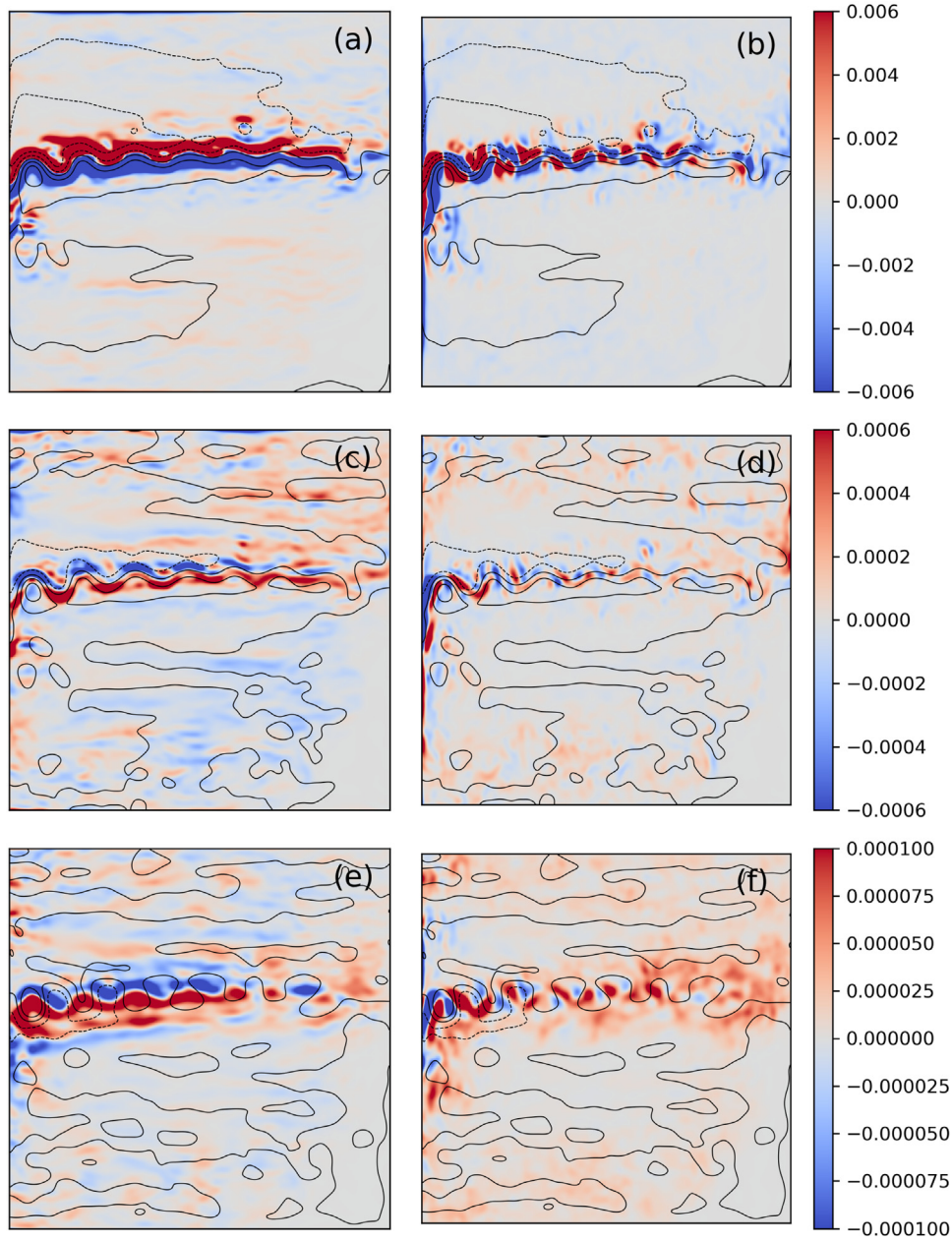
Fig. 7. The time-mean thickness EIV $\boldsymbol{u}_*^h$ in the upper (a, b), middle (c, d) and lower (e, f) layers. The zonal components of $\boldsymbol{u}_*^h$ are in panels (a, c, e) and the meridional components are in panels (b, d, f). In these plots we restrict the plotting range to grid points that are at least one half of the filter's width away form the boundaries, as only in this sub-region can we obtain $\boldsymbol{u}_*^h$ without introducing errors. Units are m^2 s^{-1} in all panels. Contours represent the time-mean large-scale streamfunction.

that advects tracers beyond $\boldsymbol{u}_*^h$. That the right-hand side of equation (2) in GM90 is not entirely diffusive can be interpreted as a reason for differences between the tracer and thickness EIVs. This is related to a more general issue of 'ambiguity' of the diffusive and advective tracer transport.

To illustrate the ambiguity issue, assume that the tracer $\overline{C}$ is advected by the rotational EIV $\boldsymbol{u}_{*r}^h$ giving the advective flux $\boldsymbol{u}_{*r}^h \overline{C}$. With our transport tensor method, a portion of this transport will in general contribute to a diffusive tracer flux and therefore not contribute to $\boldsymbol{u}_*^g$ or $\boldsymbol{u}_*^c$. We show this by considering the eddy tracer flux decomposition into components along and across the large-scale gradient,

$$\boldsymbol{f} = a\nabla\overline{C} + b\,\hat{\boldsymbol{z}} \times \nabla\overline{C}, \qquad (35)$$

for scalars a and b. If performed for two tracers, it can be shown that the diagonal entries of $\boldsymbol{K}$ (using the solution (17)) are non-zero if one or both of the tracer fluxes have a component down its respective

large-scale tracer gradient. Thus, the hypothetical flux $\boldsymbol{u}_{*r}^h \overline{C}$, or just its divergent part, will be parameterised as being partially diffusive. Some studies (Eden et al., 2007; Eden and Greatbatch, 2009; Eden, 2010) use the gradient decomposition (35) to distinguish between diffusive and advective fluxes. Our method with a transport tensor is more general and permits diffusive fluxes to have a component perpendicular to the large-scale tracer gradient. In the context of a given transport tensor $\boldsymbol{K}$, the separation of $\boldsymbol{K}$ into symmetric and antisymmetric parts separates the flux into diffusive and advective parts. However, the gradient decomposition in (35) presents a second option for defining this separation, such that for a given flux its advective and diffusive parts are not unique.

The factor of two difference between the rotational EIVs $\boldsymbol{u}_*^g$ and $\boldsymbol{u}_{*r}^h$ is caused by the above-described ambiguity of the eddy transport: some tracer transport by $\boldsymbol{u}_{*r}^h$ is quantified as being diffusive. The relationship between $(\boldsymbol{u}_*^c, \boldsymbol{u}_*^g)$ with $(\boldsymbol{u}_*^h, \boldsymbol{u}_{*r}^h)$ is likely also weakened by the fact that
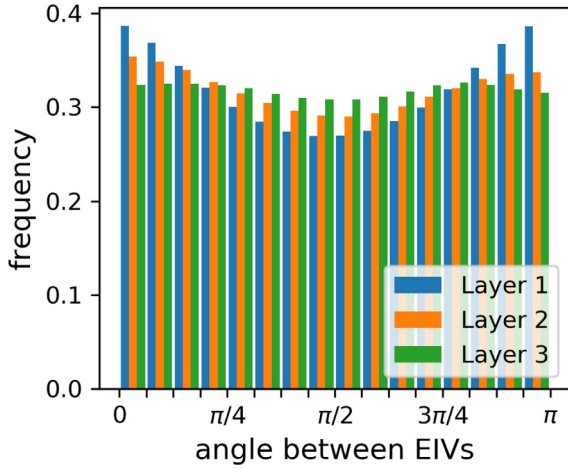
Fig. 8. Histograms of the angles between the EIVs u_*^c and u_*^h in the upper (blue), middle (orange) and lower (green) layers. The data are accumulated over one year and all grid points that lie at least one filter's width (15 grid points) away from the boundaries since here the filter commutes with the derivative, permitting diagnosis of the full u_*^h.

a fraction of the eddy variability is 'incoherent', effectively random. This incoherence is particularly strong since our eddy fluxes are not averaged and, given that the eddies are stronger in the upper layer, could contribute to a weaker relationship between tracer and thickness EIVs near the surface. A technical factor that can contribute to differences between u_*^h and u_*^c is the removal of the rotational eddy tracer flux: it is possible that eddies that contribute u_*^h do not contribute to u_*^c because the associated tracer fluxes are rotational. Another technical factor is the dependence on the tracer pairs in the inversion for K, i.e., non-uniqueness. Since u_*^c depends on the tracers, we cannot assume that mass transport would be parameterised by the same EIV, especially considering that thickness obeys different dynamics. See Section 6 for further discussion of non-uniqueness.

4.4. Relation with the large-scale flow and the GM90 parameterisation

For the purposes of parameterising missing eddy effects in coarse-resolution GCMs, it is necessary to quantify the relationship between eddy tracer transport and the large-scale flow. We seek a relationship with combinations of the large-scale shear deformation $\overline{\theta}$, stretching deformation $\overline{\sigma}$ and relative vorticity $\overline{\zeta}$:

$$\overline{\theta} = \overline{u}_y + \overline{v}_x, \quad \overline{\sigma} = \overline{u}_x - \overline{v}_y, \quad \overline{\zeta} = \overline{v}_x - \overline{u}_y. \tag{36}$$

We additionally considered large-scale PV, thickness and their gradients, but these did not perform better. The companion paper HSMB21 showed that the Frobenius norms of the transport and diffusion tensors, $\|K\|$ and $\|S\|$, are positively correlated with the strain magnitude $(\overline{\theta}^2 + \overline{\sigma}^2)^{1/2}$ and more strongly with $\Omega = \|\nabla \overline{u}\| = (\overline{\theta}^2 + \overline{\sigma}^2 + \overline{\zeta}^2)^{1/2}$ (correlations of ~ 0.6 in the lower layer).

HSMB21 also noted that K and the transpose of the large-scale velocity gradient tensor $(\nabla \overline{u})^T$ are negatively correlated, most strongly in the lower layer with entry-wise correlations roughly between -0.1 and -0.4. The correlations are weaker in the layers above, with largest correlations ~ 0.2 in the middle layer and ~ 0.1 in the upper layer. The approximate relation $K \propto -(\nabla \overline{u})^T$ implies for the eddy tracer flux $f_{\text{div}} \propto (\nabla \overline{u})^T \nabla \overline{C}$. Such a closure is not entirely new, with equivalent closures proposed for Reynolds stresses (Meneveau and Katz, 2000), eddy vorticity fluxes (Eyink, 2001) and eddy PV fluxes (Nadiga, 2008). The implied approximation for the EIV streamfunction is $A \propto \overline{\zeta}$.

In Fig. 10(a) we show a 2D histogram of A versus $\overline{\zeta}$ in the lower layer (evaluated over all grid points and one year), where the correlation between them is 0.38. For a given $\overline{\zeta}$-value, A is approximately

normally distributed, suggesting that a stochastic parameterisation for A conditioned on $\overline{\zeta}$ might be a suitable approach for parameterising the advective eddy tracer transport. Fig. 10(b) shows a 2D histogram of the magnitude $|A|$ versus Ω in the lower layer, which have a correlation of 0.55. Other rotationally invariant measures, such as the strain magnitude, have marginally weaker correlations. In the middle and upper layers the relationships become even weaker. For example, in the upper layer the correlation between A and $\overline{\zeta}$ is 0.25 and the correlation between $|A|$ and Ω is 0.44.

Although we observe weak relationships, it is nonetheless an informative result that they exist. We have sought a relationship using strict point-wise correlations, while for the purpose of parameterisation such precision may not be necessary. It may also be the case that time-lagged correlations are more suitable. Our search did not exhaust all possible large-scale features; the only nonlinear terms considered were quadratic combinations of $\overline{\theta}$, $\overline{\sigma}$ and $\overline{\zeta}$ (and PV and thickness gradients). More complicated combinations of velocity gradients, such as in Anstey and Zanna (2017), may be required for a more accurate closure. To seek these complicated relations, methods such as convolutional neural networks (Bolton and Zanna, 2019) or relevance vector machines (Zanna and Bolton, 2020) could be employed.

We now consider how the EIVs, u_*^c, u_{*d}^h and u_*^h, align with (i) the large-scale velocity vector $\overline{u}$, (ii) the large-scale relative vorticity (RV) gradient $\nabla \overline{\zeta}$ and (iii) the large-scale thickness gradient $\nabla \overline{h}$. Histograms of the angles between these vectors and the EIVs in the upper layer are shown in Fig. 11. When comparing the orientation of the time-mean EIVs with the time-mean large-scale fields, we find that the relationships presented in Fig. 11 are much stronger (not shown). Similarly, at depth the alignment tendencies are marginally stronger than those we show in Fig. 11.

The tracer EIV u_*^c tends to be oriented against the large-scale velocity. Similarly, some studies (e.g., McDougall and McIntosh, 1996, 2001; Eden, 2010) which use a Reynolds eddy decomposition find that the EIV opposes the mean flow and accordingly refer to the sum $\overline{u} + u_*^c$ (or equivalently for thickness $\overline{u} + u_*^h$) as a 'residual' velocity. That the EIVs oppose the mean flow for Reynolds eddies is a consequence of mean and eddy advections balancing each other in a steady state, but for spatial filter eddies this balance need not be satisfied at a given instant. Since the large-scale flow is often perpendicular to the RV and thickness gradients, we find that u_*^c is also often oriented perpendicular to them. This is equivalent to A contours being aligned with the large-scale RV contours. We conclude that large-scale features considered can predict the orientation of u_*^c and are best at predicting the magnitude in the lower layer. On the full thickness EIV u_*^h, we find it is most often oriented in the same direction as $\overline{u}$ but is almost as likely to be oriented in the opposite direction, and is most often perpendicular to $\nabla \overline{\zeta}$ and $\nabla \overline{h}$.

The divergent thickness EIV u_{*d}^h is much more weakly related to the large-scale flow in comparison to u_*^c and u_*^h. We find u_{*d}^h is most likely oriented down the large-scale thickness gradient, but is almost as likely to be oriented up this gradient. There is an important link here with the GM90 parameterisation. For use in primitive equation models GM90 and Gent et al. (1995) proposed a specific form for u_*^h which was a three-dimensional non-divergent velocity field dependent on the isopycnal slope. In isopycnal coordinates the (horizontal) velocity is

$$u_*^{GM} = -\frac{1}{\overline{h}} \partial_\rho \left(\kappa \nabla \overline{\eta} \right), \tag{37}$$

where ρ is the density and η is the height of an isopycnal surface, related to the thickness via $\partial_\rho \eta = h$. For a continuously stratified ocean, ∂_ρ represents the continuous derivative with respect to density, whereas in a layered model it represents a discrete difference. The parameter κ, introduced by GM90 as the 'thickness diffusivity', in general depends on x, y, t and ρ. If κ were independent of ρ then the parameterised flux $u_*^{GM} \overline{h}$ would be oriented down the thickness gradient, with κ being a scalar diffusivity coefficient. In general, though, the flux has both skew and down-gradient components. In this study we do not test the efficacy
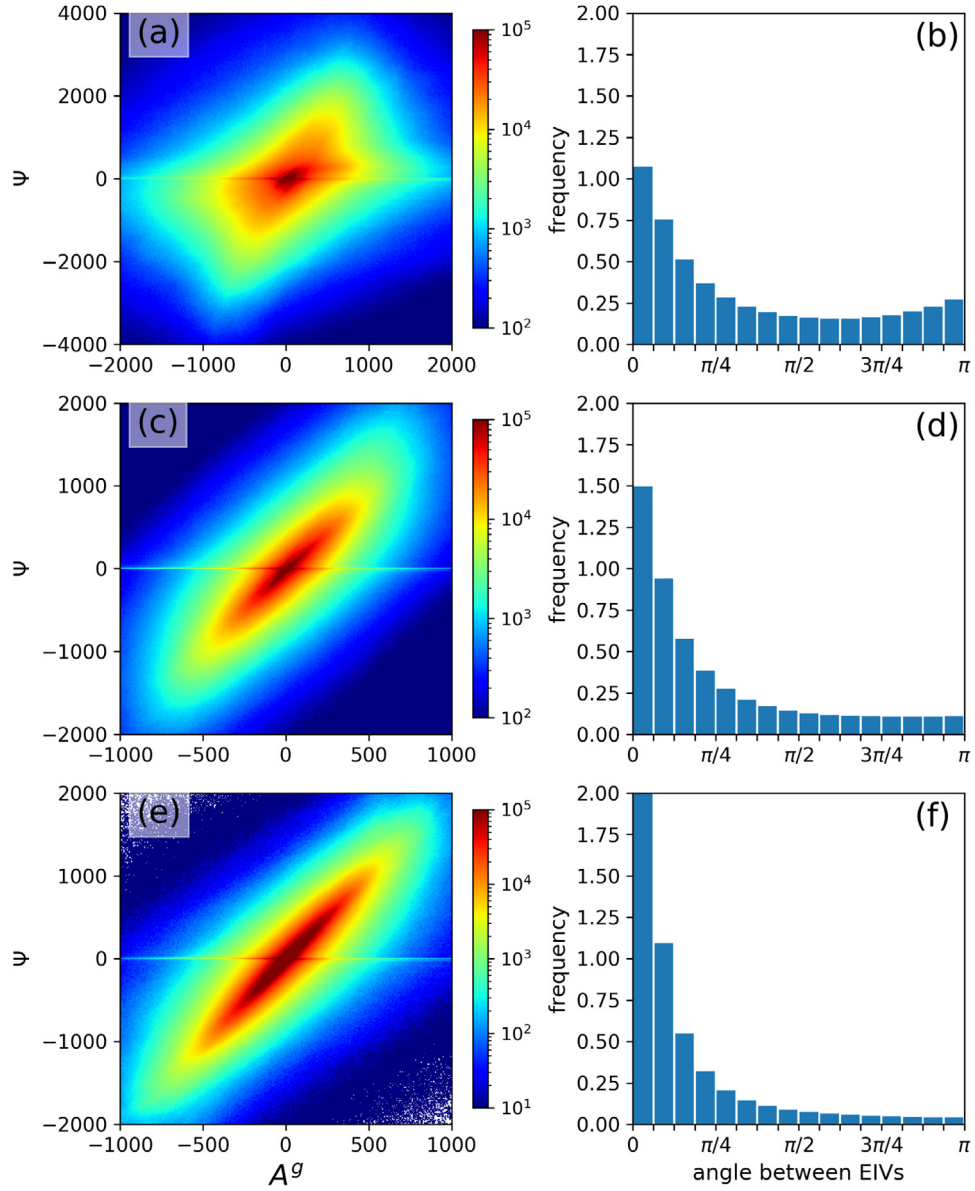
Fig. 9. (a, c, e) 2D histograms of A^g and Ψ. Units for both axes are m^2 s^{-1}. (b, d, f) Histograms of the angle between the portion of the tracer EIV $\boldsymbol{u}^g_*$ and the rotational thickness EIV $\boldsymbol{u}^h_{*r}$. Frequency units are arbitrary. Results are for the upper layer (a, b), middle layer (c, d) and lower layer (e, f).
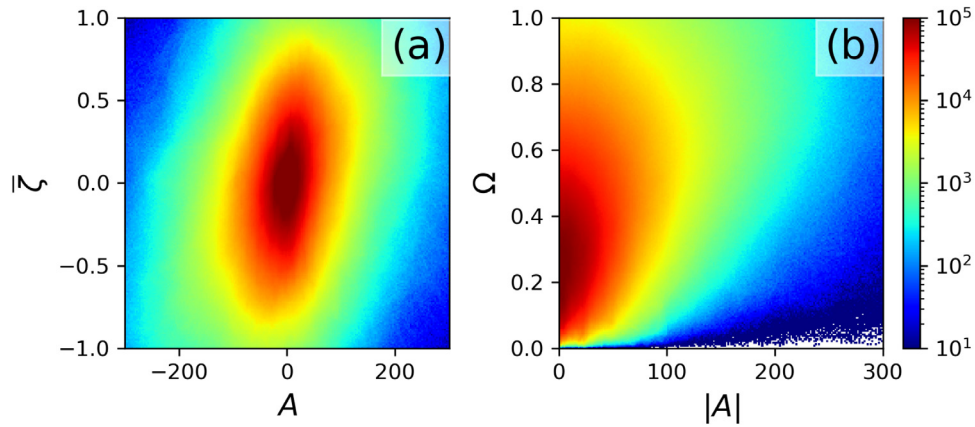

Fig. 10. 2D histograms of (a) the tracer EIV streamfunction A versus the large-scale relative vorticity $\bar{\zeta}$ (correlation 0.38) and (b) $|A|$ versus the strain–vorticity magnitude $\Omega = (\bar{\theta}^2 + \bar{\sigma}^2 + \bar{\zeta}^2)^{1/2}$ (correlation 0.55). Units for A and $|A|$ on the x-axes are m^2 s^{-1}. Both $\bar{\zeta}$ and Ω on the y-axes have been rescaled and have arbitrary dimensionless units. Data is aggregated over one year and all grid points.
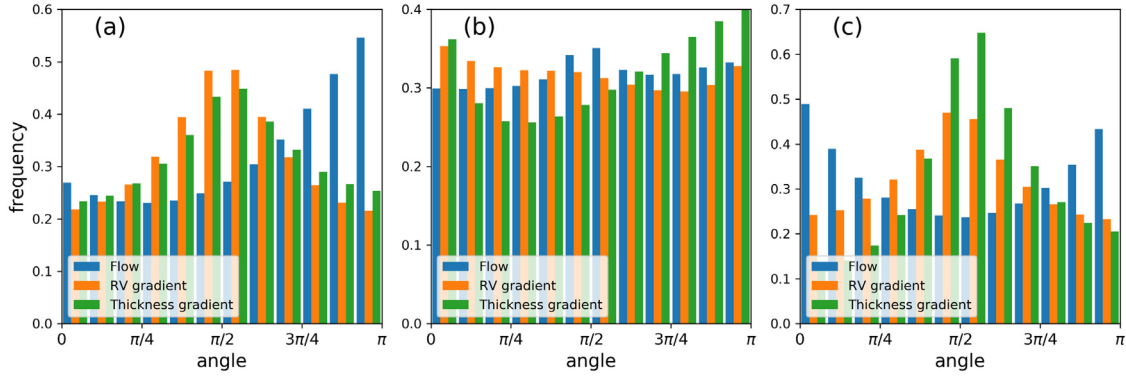
Fig. 11. Histograms of the angles between the EIVs and (i, blue) the large-scale velocity vector, (ii, orange) the large-scale RV gradient and (iii, green) the large-scale thickness gradient. (a) The angle between the instantaneous large-scale flow properties and the instantaneous tracer EIV $\boldsymbol{u}^c_*$, evaluated over one year. (b) Angles for the divergent thickness EIV $\boldsymbol{u}^h_{*d}$. (c) Angles for the thickness EIV $\boldsymbol{u}^h_*$ evaluated over all grid points at least one half of the filter's width away from the boundaries. Data is presented for the upper layer; results in the lower layers exhibit similar but slightly stronger tendencies.

of any closure for $\boldsymbol{u}^{GM}_*$; to do so requires inversion of the differential equation (37) for κ.

The motivation for the closure in (37) is to parameterise the potential energy-releasing effects of baroclinic instability, achieved by down-gradient fluxes which flatten isopycnal interfaces. With $\boldsymbol{u}^h_{*d}$ exhibiting a weak tendency to be oriented down the large-scale thickness gradient, our results imply $\boldsymbol{u}^h_{*d}$ partly accounts for the same potential energy-releasing effects. In isopycnal coordinates $\boldsymbol{u}^{GM}_*$ has both rotational and divergent components, and so cannot be exactly identified with $\boldsymbol{u}^h_{*d}$. On top of this, a subtlety of (37) is that the eddy mass flux is a density derivative of the interface height flux, not the thickness flux. The sea-surface height anomaly is proportional to ψ_1 so upper-layer alignments between the EIVs and the large-scale interface height gradient $\nabla\overline{\eta}$ can be inferred from the alignments with the large-scale velocity vector $\overline{\boldsymbol{u}}$. Fig. 11(b) shows that $\boldsymbol{u}^h_{*d}$ has a weak tendency to be perpendicular to $\overline{\boldsymbol{u}}$, and by extension tends to be oriented down the gradient of the $\nabla\overline{\eta}$ in addition to that of large-scale thickness. GM90 was not focused on QG flow or spatial filter decompositions, which can explain differences between our thickness EIVs and $\boldsymbol{u}^{GM}_*$.

In the GM90 parameterisation $\boldsymbol{u}^{GM}_*$ advects passive tracers in addition to mass. In this study we have diagnosed distinct tracer and thickness EIVs, which indicates that the transport by $\boldsymbol{u}^h_*$, or indeed $\boldsymbol{u}^{GM}_*$, does not account for all eddy tracer advection. The difference $\boldsymbol{u}^c_* - \boldsymbol{u}^h_*$ represents an incremental EIV that advects tracers beyond the thickness-determined $\boldsymbol{u}^h_*$. The tracer transport R-term in GM90 (cf. equation (2)) was assumed to be diffusive, whereas our analysis indicates that it may also have an along-isopycnal advection component.

5. Results for Reynolds eddies

Here we consider results for eddies defined as the deviation from the time mean, which we refer to as *Reynolds eddies*. Given a field $\phi = \phi(x, y, t)$, its temporal Reynolds decomposition is

$$\phi(x, y, t) = \langle\phi\rangle(x, y) + \phi^\#(x, y, t),\qquad(38)$$

where $\langle\phi\rangle$ is its time mean and $\phi^\#$ is the deviation from the time mean. The corresponding flux-gradient relation is

$$\langle\boldsymbol{u}^\# C^\#\rangle_{\text{div}} = -\boldsymbol{K}^{\text{Reyn}}\nabla\langle C\rangle,\qquad(39)$$

where $\boldsymbol{K}^{\text{Reyn}}(x, y)$ is the transport tensor for Reynolds eddies and $\langle\boldsymbol{u}^\# C^\#\rangle_{\text{div}}$ is the divergent part of the time-mean eddy tracer flux. We denote the diffusion and advection tensors as $\boldsymbol{S}^{\text{Reyn}}$ and $\boldsymbol{A}^{\text{Reyn}}$, respectively, which are the symmetric and antisymmetric parts of $\boldsymbol{K}^{\text{Reyn}}$. The off-diagonal element $A^{\text{Reyn}} = -A^{\text{Reyn}}_{12} = A^{\text{Reyn}}_{21}$ is the streamfunction for the EIV $\boldsymbol{u}^{\text{Reyn}}_*(x, y)$.

The elements of $\boldsymbol{K}^{\text{Reyn}}$ are shown in HSMB21, so we do not repeat them here. HSMB21 discussed how there are clear similarities with K_{12}

and K_{21} for spatially filtered eddies, but there are also some important differences, most notably that $\boldsymbol{K}^{\text{Reyn}}$ and its symmetric/antisymmetric parts are at least twice as large as the corresponding tensors for spatially filtered eddies. On qualitative features, although we broadly have that K^{Reyn}_{21} is positive/negative to south/north of the jet, there is not a coherent change of sign on the jet core, unlike with $\langle K_{21}\rangle$. This means that the divergent eddy tracer flux for Reynolds eddies does not exhibit the same divergence pattern on the jet core and its flanks. In the lower layers $\boldsymbol{K}^{\text{Reyn}}$ and $\langle\boldsymbol{K}\rangle$ are much more similar. It is also important to note that differences between $\langle C\rangle$ and $\overline{C}$ can also cause differences between the eddy fluxes for Reynolds and spatial filter eddies.

In Fig. 12 we show A^{Reyn} in each layer, to be compared with Fig. 2 in which we show the time-mean A for spatial filter eddies. In the jet region of all layers, A^{Reyn} and $\langle A\rangle$ are both broadly positive/negative to the south/north of the jet core. However, as discussed previously, the upper layer $\langle A^{\text{Reyn}}\rangle$ has relatively convoluted behaviour on the jet core so its corresponding EIV is not a coherent along-jet velocity. Away from the jet, in all layers we do not observe any distinct qualitative features shared between A^{Reyn} and $\langle A\rangle$. The corresponding EIV speeds (not shown) for A^{Reyn} and $\langle A\rangle$ are only of similar amplitude in the jet region of the upper two layers, whereas elsewhere the EIV for space-filtered eddies is an order of magnitude larger. There is a weak tendency for $\langle\boldsymbol{u}^c_*\rangle$ and $\boldsymbol{u}^{\text{Reyn}}_*$ to be oriented in the same direction.

Our main conclusion here is that the transport tensors for Reynolds and spatial filter eddies are distinct, leading to disparities in both the associated diffusive and advective tracer fluxes. The most notable difference is that $\boldsymbol{K}^{\text{Reyn}}$ is roughly twice $\langle\boldsymbol{K}\rangle$ in amplitude. Qualitative differences are most pronounced in the most energetic areas of the domain, such as the upper-layer jet.

6. Conclusion

Isopycnal eddy fluxes of passive tracers can be parameterised by a transport tensor $\boldsymbol{K}$ acting upon the large-scale tracer gradient. A key step in any study of eddy transport is defining the large-scale and small-scale (eddy) fields. It is most common for studies to use either a zonal or temporal Reynolds mean (Medvedev and Greatbatch, 2004; Eden et al., 2007; Eden and Greatbatch, 2009; Eden, 2010; Bachman and Fox-Kemper, 2013; Bachman et al., 2015, 2017b, 2020) and define eddies as the deviation. In this study we instead use a spatial filter to separate the scales which has multiple advantages over the Reynolds decomposition. First, with a spatial filter the large-scale fields have full spatio-temporal dependence which is suitable since fields in a coarse-resolution ocean model will always have such dependence. Second, it is possible for mesoscale eddies to be stationary (Lu et al., 2016), and these would always be contained in the large-scale fields if temporal Reynolds averaging is used, but would not be simulated by coarse-resolution ocean models. Third, as eddy-permitting and eddy-resolving
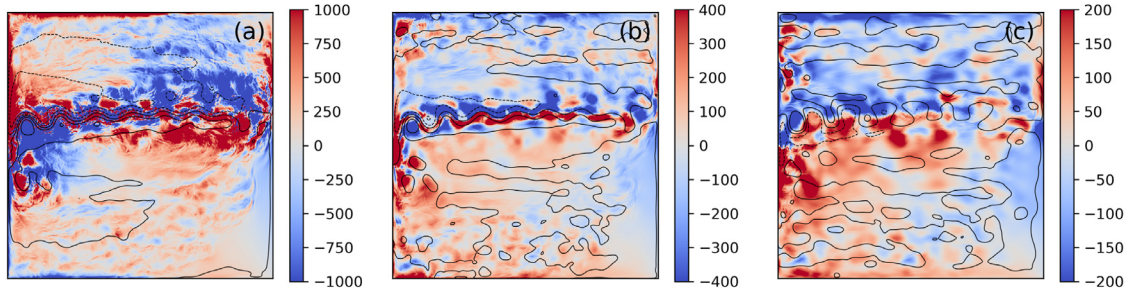
Fig. 12. The off-diagonal advection tensor component $A^{\text{Reyn}}(=-A_{12}^{\text{Reyn}}=A_{21}^{\text{Reyn}})$ in the (a) upper, (b) middle and (c) lower layers for Reynolds-averaged eddies. Units are m^2 s^{-1}.

ocean models become more viable, Reynolds averaging approaches become more unviable as the separation of time scales between resolved and unresolved flows diminishes (Nadiga, 2008).

By separating K into its symmetric (S) and antisymmetric (A) parts we separate the eddy tracer flux into its diffusive and advective components. The precursor to the present study Haigh et al. (2021) focused on the diffusion tensor S, whereas in the present study we focused on the advection tensor A. We refer to A as the advection tensor since its associated tracer forcing can be expressed as advection of the large-scale tracer field by a non-divergent *eddy-induced velocity* (EIV), $\boldsymbol{u}_*^c$. The off-diagonal component of A, namely $A = -A_{12} = A_{21}$, is the streamfunction for $\boldsymbol{u}_*^c$. We find that speeds associated with $\boldsymbol{u}_*^c$ are up to 1 m s^{-1} near the jet in the upper layer and are on the order of 0.01 m s^{-1} elsewhere in the upper layer. In the layers below $\boldsymbol{u}_*^c$ speeds are typically on the order of 0.001 m s^{-1}. Overall, the non-negligible speeds indicate that the advective flux plays a significant role in tracer transport.

Using the Gent and McWilliams (1990) (hereafter GM90) framework, eddy transport of mass in ocean models is parameterised by including an extra advection by an EIV. The same EIV is used to advect passive tracers, with the remainder of eddy effects on tracers assumed to be diffusive. The same formulation can be derived for the QG, spatial filter model that we use in this study, as shown in Appendix A. We diagnose the isopycnal thickness EIV $\boldsymbol{u}_*^h$ using the GM90 framework (noting the thickness EIV cannot be diagnosed globally due to the filter operator not commuting with the derivative operator) and find it is not similar to the tracer EIV $\boldsymbol{u}_*^c$. Specifically, the EIVs do not show a significant tendency to be oriented in the same direction and $\boldsymbol{u}_*^c$ is typically three to six times larger than $\boldsymbol{u}_*^h$. The divergent part $\boldsymbol{u}_{*d}^h$ of the thickness EIV is two orders of magnitude smaller than the tracer EIV $\boldsymbol{u}_*^c$ and is negligible for tracer transport. Technical issues prevent the diagnosis of the entire rotational part of $\boldsymbol{u}_*^h$, but a rotational portion $\boldsymbol{u}_{*r}^h$ can be obtained from the unfiltered eddy mass flux $\boldsymbol{g}^h = \overline{\boldsymbol{u}}h' + \boldsymbol{u}'\overline{h} + \boldsymbol{u}'h'$. The corresponding portion of the tracer EIV $\boldsymbol{u}_*^g$ can be obtained from the unfiltered eddy tracer flux $\boldsymbol{g}^c = \overline{\boldsymbol{u}}C' + \boldsymbol{u}'\overline{C} + \boldsymbol{u}'C'$. These EIVs, $\boldsymbol{u}_*^g$ and $\boldsymbol{u}_{*r}^h$ which are derived from like terms in their respective budgets, share qualities in common but are nonetheless fundamentally different.

The differences between the tracer- and thickness-determined EIVs imply that the advective eddy tracer transport cannot be determined solely from mass analysis, and that $\boldsymbol{u}_*^c - \boldsymbol{u}_*^h$ represents the incremental EIV that advects tracers beyond the thickness-determined $\boldsymbol{u}_*^h$. That passive tracers are advected by an EIV beyond the thickness-determined EIVs does not contradict GM90 with regard to role of the thickness EIV. It does, however, contradict the assumption regarding their R-term (cf. equation (2)), which was assumed to include only diffusive effects. The issue remains to parameterise the tracer EIV $\boldsymbol{u}_*^c$, which requires expressing it in terms of large-scale (resolved) flow features. We found that $\boldsymbol{u}_*^c$ tends to be perpendicular to the gradients of large-scale thickness and relative vorticity and counter to the large-scale flow. The streamfunction A for the EIV $\boldsymbol{u}_*^c$ exhibits a broad and approximate normal distribution when conditioned on the large-scale relative vorticity, $\overline{\zeta}$, suggesting that a stochastic closure for A is most suitable.

One issue little discussed in this study is *non-uniqueness* of the transport tensor K, that is, a dependence of K on the choice of tracers and their gradients (Sun et al., 2021; Kamenkovich et al., 2021). We have focused on results for a specific tracer pair, for which K exhibits strong space–time variability. We additionally diagnosed K for a pair of wave-like tracer fields and found that, although the new K is not exactly the same, none of our conclusions change. We hypothesise that the non-uniqueness and variability of K is due to two factors that require further study:

(1) eddies in the ocean can induce *chaotic advection* of passive tracers (Pierrehumbert, 1991); this leads to K being a stochastic object, with specific realisations dependent on the eddy and tracer fields;

(2) the flux-gradient relation (16) is an *incomplete model* of eddy transport, meaning that eddy fluxes may depend on components of the large-scale tracer field other than its gradient, such as the local curvature field $\nabla\nabla\overline{C}$, or the tracer history.

We argue that the transport tensor representation of eddy tracer fluxes is best viewed as sampled from a random distribution that expresses the underlying chaos and/or incompleteness. Importantly, this does not contradict the view that the K-distribution and the dynamics that generate it are independent of C.

In this study we use a QG model to predict tracer and mass eddy fluxes. Our conclusions are intended to have implications for more complete, e.g., primitive equation, models, and are intended to inform future mesoscale eddy parameterisations. While QG can be and is successfully applied outside of its formal limits of applicability (Mundt et al., 1997; Zurita-Gotor and Vallis, 2009; Shevchenko and Berloff, 2015) – so that its solutions are highly applicable to primitive equation models – a natural extension of this work would be to repeat the analyses with a primitive equation model.

Declaration of competing interest

Acknowledgements

Appendix A. An alternative tracer equation

[Gent and McWilliams (1990)](#) and [Gent et al. (1995)](#) presented a tracer equation for the primitive equations in which the tracer is explicitly advected by the thickness EIV. In this appendix we present the analogous tracer equation for our quasigeostrophic model and spatial filter scale separation.

We start by combining the tracer equation (8) and the thickness equation (23) to give

$$\frac{\partial(hC)}{\partial t} + \nabla \cdot (\boldsymbol{u}hC) + CH\nabla \cdot \boldsymbol{u}_a = 0. \tag{40}$$

Then we express hC in terms of eddy and large-scale parts:

$$hC = \overline{h}\,\overline{C} + h'\overline{C} + \overline{h}C' + h'C' = \overline{h}\,\overline{C} + g_{h,C} \quad \text{where} \quad g_{h,C} = h'\overline{C} + \overline{h}C' + h'C'. \tag{41}$$

We do the same for $\boldsymbol{u}hC$ to get

$$\boldsymbol{u}hC = \overline{\boldsymbol{u}h}\,\overline{C} + g_{uh,C} \quad \text{where} \quad g_{uh,C} = (\boldsymbol{u}h)'\overline{C} + \overline{\boldsymbol{u}h}C' + (\boldsymbol{u}h)'C'. \tag{42}$$

Then, with the eddy thickness flux defined as $\boldsymbol{f}^h = \overline{\boldsymbol{u}h} - \overline{\boldsymbol{u}}\overline{h}$ (neglecting non-commutativity of the filter and the derivative near the boundaries), we have

$$\boldsymbol{u}hC = \overline{\boldsymbol{u}}\,\overline{h}\,\overline{C} + \boldsymbol{f}^h\overline{C} + g_{uh,C}. \tag{43}$$

Substituting (41) and (43) into (40) gives

$$\frac{\partial(\overline{h}\,\overline{C})}{\partial t} + \frac{\partial g_{h,C}}{\partial t} + \nabla \cdot \left(\overline{\boldsymbol{u}}\,\overline{h}\,\overline{C} + \boldsymbol{f}^h\overline{C} + g_{uh,C}\right) + CH\nabla \cdot \boldsymbol{u}_a = 0. \tag{44}$$

Substituting the filtered thickness equation (24) into (44) gives

$$\overline{h}\frac{\partial\overline{C}}{\partial t} - \overline{C}\left[\nabla\cdot\left(\overline{\boldsymbol{u}}\overline{h}\right) + \nabla\cdot\boldsymbol{f}^h + H\overline{\nabla\cdot\boldsymbol{u}_a}\right] + \nabla\cdot\left(\overline{\boldsymbol{u}}\overline{h}\,\overline{C} + \boldsymbol{f}^h\overline{C}\right)$$
$$= -\frac{\partial g_{h,C}}{\partial t} - \nabla\cdot g_{uh,C} - CH\nabla\cdot\boldsymbol{u}_a \tag{45}$$
$$\implies \frac{\partial\overline{C}}{\partial t} + \left(\overline{\boldsymbol{u}} + \frac{\boldsymbol{f}^h}{\overline{h}}\right)\cdot\nabla\overline{C} = -\frac{1}{\overline{h}}\frac{\partial g_{h,C}}{\partial t} - \frac{1}{\overline{h}}\nabla\cdot g_{uh,C}$$
$$+ \frac{H}{\overline{h}}\left(\overline{C}\,\overline{\nabla\cdot\boldsymbol{u}_a} - C\nabla\cdot\boldsymbol{u}_a\right). \tag{46}$$

Here $\boldsymbol{f}^h/\overline{h} = \boldsymbol{u}_*^h$ is the eddy thickness EIV which advects the passive tracer.

For a standard Reynolds eddy decomposition the terms $g_{h,C}$ and $g_{uh,C}$ would instead be single eddy–eddy interaction terms, but ours include two additional large-scale/eddy interaction contributions. We also have the extra ageostrophic velocity term which accounts for the fact that a $\boldsymbol{u}_a$ term affects mass but not tracers. Studies typically neglect the $\partial g_{h,C}/\partial t$ term and as per GM90 assume that the remainder of the terms on the right-hand side are purely diffusive.

Appendix B. An analytical model for A^g

Here we present a simple analytical model which can explain the approximate relationship $\Psi \approx 2A^g \approx \psi'$, where ψ' is the streamfunction for the eddy velocity $\boldsymbol{u}'$. These approximations are accurate in the lower layer, but are much less so in the upper layer. First recall that A^g is the streamfunction for the tracer EIV associated with the $\boldsymbol{g} = \overline{\boldsymbol{u}}C' + \boldsymbol{u}'\overline{C} + \boldsymbol{u}'C'$ portion of the full eddy tracer flux. It is precisely the tracer flux contribution $\boldsymbol{u}'\overline{C}$ and the mass flux contribution $\boldsymbol{u}'H$ – which are most dominant at depth – that are responsible for the approximate relationship $\Psi \approx 2A^g \approx \psi'$, where the other components of the eddy fluxes are more important, such as in the upper layer, the approximation is less valid. We will denote the transport tensor and EIV streamfunction associated with the flux $\boldsymbol{u}'\overline{C}$ as $\hat{K}$ and $\hat{A}$, respectively.

With regard to the eddy mass flux, it is trivial that the streamfunction for the rotational flux $\boldsymbol{u}'H$ is $\psi'H$. For the eddy tracer flux, we use an idealised analytical example in a domain with no boundaries. Assume we have two large-scale tracer fields with exactly linear profiles

— for simplicity we take $\overline{C}_1 = \chi x$ and $\overline{C}_2 = \gamma y$, where χ and γ are constants. Since the transport tensor is the same for all linear tracers, we are able to focus on two particular linear tracer fields without loss of generality. Substitution of the tracer gradients χ and γ into (17) yields the expression for the transport tensor,

$$\hat{K} = -\begin{pmatrix} f_1^{(u)}/\chi & f_2^{(u)}/\gamma \\ f_1^{(v)}/\chi & f_2^{(v)}/\gamma \end{pmatrix}, \tag{47}$$

where $(f_1^{(u)}, f_1^{(v)})$ and $(f_2^{(u)}, f_2^{(v)})$ are the divergent fluxes for the two tracers.

To proceed we assume a suitable form for the velocity $\boldsymbol{u}'$ and streamfunction ψ'. We consider two options in tandem, a 'wave-like' flow and an 'eddy-like' flow with streamfunctions

$$\psi' = \cos(kx + ly) \quad \text{and} \quad \psi' = \sin(kx)\sin(ly), \tag{48}$$

respectively, with zonal and meridional wavenumbers k and l. It can be shown that for both flows the divergent potentials for the fluxes $\boldsymbol{u}'\overline{C}_1 = \boldsymbol{u}'\chi x$ and $\boldsymbol{u}'\overline{C}_2 = \boldsymbol{u}'\gamma y$ are

$$\phi_1 = -\chi\kappa^{-2}u' \quad \text{and} \quad \phi_2 = -\gamma\kappa^{-2}v', \tag{49}$$

respectively, where $\kappa = \sqrt{k^2 + l^2}$. Since the above is true for both the wave-like and the eddy-like flow fields, we do not distinguish between the two and the notation $(u', v') = (-\psi'_y, \psi'_x)$ applies to both options. With these divergent potentials, the divergent fluxes are

$$(f_1^{(u)}, f_1^{(v)}) = -\chi\kappa^{-2}\nabla u' \quad \text{and} \quad (f_2^{(u)}, f_2^{(v)}) = -\gamma\kappa^{-2}\nabla v'. \tag{50}$$

Substituting these into (47) we find that the transport tensor for the idealised $\boldsymbol{u}'\overline{C}$ flux is

$$\hat{K} = \kappa^{-2}\left(\nabla\boldsymbol{u}'\right)^T = \kappa^{-2}\begin{pmatrix} u'_x & v'_x \\ u'_y & v'_y \end{pmatrix}, \tag{51}$$

i.e., it is the transpose of a velocity gradient matrix. The symmetric part of $\hat{K}$ is proportional to the strain-rate matrix for the velocity $\boldsymbol{u}'$ and has eigenvalues that are equal and opposite — such opposite-signed eigenvalues was a key finding of the counterpart study [Haigh et al. (2021)](#). The antisymmetric part of $\hat{K}$ is uniquely defined by its off-diagonal component $\hat{A} = -\hat{A}_{12} = \hat{A}_{21}$. We find that

$$\hat{A} = -\frac{1}{2}\kappa^{-2}\left(v'_x - u'_y\right) = -\frac{1}{2}\kappa^{-2}\zeta' = \frac{1}{2}\psi'. \tag{52}$$

We remind that this only applies to the $\boldsymbol{u}'\overline{C}$ flux, and does not tell us anything about the other components of the eddy tracer flux.

References

Andrews, D.G., McIntyre, M.E., 1978. Generalized Eliassen-Palm and Charney-Drazin theorems for waves on axisymmetric mean flows in compressible atmospheres. J. Atmos. Sci. (ISSN: 0022-4928) 35 (2), 175–185. http://dx.doi.org/10.1175/1520-0469(1978)035<0175:GEPACD>2.0.CO;2.

Anstey, J.A., Zanna, L., 2017. A deformation-based parametrization of ocean mesoscale eddy reynolds stresses. Ocean Model. (ISSN: 1463-5003) 112, 99–111. http://dx.doi.org/10.1016/j.ocemod.2017.02.004.

Bachman, S.D., 2019. The GM + E closure: A framework for coupling backscatter with the Gent and McWilliams parameterization. Ocean Model. (ISSN: 1463-5003) 136, 85–106. http://dx.doi.org/10.1016/j.ocemod.2019.02.006.

Bachman, S.D, Fox-Kemper, B., 2013. Eddy parameterization challenge suite I: Eady spindown. Ocean Modell. (ISSN: 1463-5003) 64, 12–28. http://dx.doi.org/10.1016/j.ocemod.2012.12.003.

Bachman, S.D., Fox-Kemper, B., Bryan, F.O., 2015. A tracer-based inversion method for diagnosing eddy-induced diffusivity and advection. Ocean Modell. (ISSN: 1463-5003) 86, 1–14. http://dx.doi.org/10.1016/j.ocemod.2014.11.006.

Bachman, S.D., Fox-Kemper, B., Bryan, F.O., 2020. A diagnosis of anisotropic eddy diffusion from a high-resolution global ocean model. J. Adv. Modelling Earth Syst. 12 (2), http://dx.doi.org/10.1029/2019MS001904, e2019MS001904.

Bachman, S.D., Fox-Kemper, B., Pearson, B., 2017a. A scale-aware subgrid model for quasi-geostrophic turbulence. J. Geophys. Res. Oceans 122 (2), 1529–1554. http://dx.doi.org/10.1002/2016JC012265.

Bachman, S.D., Marshall, D.P., Maddison, J.R., Mak, J., 2017b. Evaluation of a scalar eddy transport coefficient based on geometric constraints. Ocean Modell. (ISSN: 1463-5003) 109, 44–54. http://dx.doi.org/10.1016/j.ocemod.2016.12.004.

Berloff, P.S., 2005. On dynamically consistent eddy fluxes. Dyn. Atmos. Oceans (ISSN: 0377-0265) 38 (3), 123–146. http://dx.doi.org/10.1016/j.dynatmoce.2004.11.003.

Berloff, P., 2018. Dynamically consistent parameterization of mesoscale eddies. Part III: Deterministic approach. Ocean Model. (ISSN: 1463-5003) 127, 1–15. http://dx.doi.org/10.1016/j.ocemod.2018.04.009.

Berloff, P.S., McWilliams, J.C., 1999. Quasigeostrophic dynamics of the western boundary current. J. Phys. Oceanogr. 29 (10), 2607–2634. http://dx.doi.org/10.1175/1520-0485(1999)029<2607:QDOTWB>2.0.CO;2.

Berloff, P., Ryzhov, E., Shevchenko, I., 2021. On dynamically unresolved oceanic mesoscale motions. J. Fluid Mech. 920, A41. http://dx.doi.org/10.1017/jfm.2021.477.

Bolton, T., Zanna, L., 2019. Applications of deep learning to ocean data inference and subgrid parameterization. J. Adv. Modelling Earth Syst. 11 (1), 376–399. http://dx.doi.org/10.1029/2018MS001472.

Chen, C., Kamenkovich, I., Berloff, P., 2016. Eddy trains and striations in quasi-geostrophic simulations and the ocean. J. Phys. Oceanogr. (ISSN: 0022-3670) 46 (9), 2807–2825. http://dx.doi.org/10.1175/JPO-D-16-0066.1.

Danabasoglu, G., McWilliams, J.C., Gent, P.R., 1994. The role of mesoscale tracer transports in the global ocean circulation. Science (ISSN: 0036-8075) 264 (5162), 1123–1126. http://dx.doi.org/10.1126/science.264.5162.1123.

Eden, C., 2010. Anisotropic rotational and isotropic residual isopycnal mesoscale eddy fluxes. J. Phys. Oceanogr. 40 (11), 2511–2524. http://dx.doi.org/10.1175/2010JPO4397.1.

Eden, C., Greatbatch, R.J., 2009. A diagnosis of isopycnal mixing by mesoscale eddies. Ocean Modell. (ISSN: 1463-5003) 27 (1), 98–106. http://dx.doi.org/10.1016/j.ocemod.2008.12.002.

Eden, C., Greatbatch, R.J., Olbers, D., 2007. Interpreting eddy fluxes. J. Phys. Oceanogr. 37 (5), 1282–1296. http://dx.doi.org/10.1175/JPO3050.1.

Eyink, G.L., 2001. Dissipation in turbulent solutions of 2D Euler equations. Nonlinearity 14 (4), 787–802. http://dx.doi.org/10.1088/0951-7715/14/4/307.

Fox-Kemper, B., Menemenlis, D., 2008. Can large eddy simulation techniques improve mesoscale rich ocean models? In: Ocean Modeling in an Eddying Regime. American Geophysical Union (AGU), ISBN: 9781118666432, pp. 319–337. http://dx.doi.org/10.1029/177GM19.

Gent, P.R., 2011. The Gent–McWilliams parameterization: 20/20 hindsight. Ocean Model. (ISSN: 1463-5003) 39 (1), 2–9. http://dx.doi.org/10.1016/j.ocemod.2010.08.002, Modelling and Understanding the Ocean Mesoscale and Submesoscale.

Gent, P.R., McWilliams, J.C., 1990. Isopycnal mixing in ocean circulation models. J. Phys. Oceanogr. 20 (1), 150–155. http://dx.doi.org/10.1175/1520-0485(1990)020<0150:IMIOCM>2.0.CO;2.

Gent, P.R., Willebrand, J., McDougall, T.J., McWilliams, J.C., 1995. Parameterizing eddy-induced tracer transports in ocean circulation models. J. Phys. Oceanogr. 25 (4), 463–474. http://dx.doi.org/10.1175/1520-0485(1995)025<0463:PEITTI>2.0.CO;2.

Griffies, S.M., 1998. The Gent–McWilliams skew flux. J. Phys. Oceanogr. 28 (5), 831–841. http://dx.doi.org/10.1175/1520-0485(1998)028<0831:TGMSF>2.0.CO;2.

Grooms, I., Kleiber, W., 2019. Diagnosing, modeling, and testing a multiplicative stochastic Gent–McWilliams parameterization. Ocean Model. (ISSN: 1463-5003) 133, 1–10. http://dx.doi.org/10.1016/j.ocemod.2018.10.009.

Haigh, M., Sun, L., McWilliams, J.C., Berloff, P., 2021. On eddy transport in the ocean. Part I: The diffusion tensor. Ocean Modell. (ISSN: 1463-5003) 164, 101831. http://dx.doi.org/10.1016/j.ocemod.2021.101831.

Haigh, M., Sun, L., Shevchenko, I., Berloff, P., 2020. Tracer-based estimates of eddy-induced diffusivities. Deep Sea Res. I: Oceanogr. Res. Pap. (ISSN: 0967-0637) http://dx.doi.org/10.1016/j.dsr.2020.103264.

Kamenkovich, I., Berloff, P., Haigh, M., Sun, L., Lu, Y., 2021. Complexity of mesoscale eddy diffusivity in the ocean. Geophys. Res. Lett. 45 (3), e2020GL091719. http://dx.doi.org/10.1029/2020GL091719, e2020GL091719 2020GL091719.

Karabasov, S.A., Berloff, P.S., Goloviznin, V.M., 2009. CABARET in the ocean gyres. Ocean Modell. (ISSN: 1463-5003) 30 (2), 155–168. http://dx.doi.org/10.1016/j.ocemod.2009.06.009.

Killworth, P.D., 1997. On the parameterization of eddy transfer Part I. Theory. J. Mar. Res. (ISSN: 0022-2402) 55 (6), 1171–1197. http://dx.doi.org/10.1357/0022240973224102.

Lau, N.C., Wallace, John M., 1979. On the distribution of horizontal transports by transient eddies in the northern hemisphere wintertime circulation'. J. Atmos. Sci. 36 (10), 1844–1861. http://dx.doi.org/10.1175/1520-0469(1979)036<1844:OTDOHT>2.0.CO;2.

Leonard, A., 1975. Energy cascade in large-eddy simulations of turbulent fluid flows. In: Frenkiel, F.N., Munn, R.E. (Eds.), Turbulent Diffusion in Environmental Pollution. In: Advances in Geophysics, vol. 18, Elsevier, (ISSN: 0065-2687) pp. 237–248. http://dx.doi.org/10.1016/S0065-2687(08)60464-1.

Lilly, D.K., 1967. The representation of small-scale turbulence in numerical simulation experiments. In: Proceedings of the IBM Scientific Computing Symposium on Environmental Sciences. pp. 195–201.

Lu, J., Wang, F., Liu, H., Lin, P., 2016. Stationary mesoscale eddies, upgradient eddy fluxes, and the anisotropy of eddy diffusivity. Geophys. Res. Lett. 43 (2), 743–751. http://dx.doi.org/10.1002/2015GL067384.

Maddison, J.R., Marshall, D.P., Shipton, J., 2015. On the dynamical influence of ocean eddy potential vorticity fluxes. Ocean Modell. (ISSN: 1463-5003) 92, 169–182. http://dx.doi.org/10.1016/j.ocemod.2015.06.003.

Marshall, J., Shutts, G., 1981. A note on rotational and divergent eddy fluxes. J. Phys. Oceanogr. 11 (12), 1677–1680. http://dx.doi.org/10.1175/1520-0485(1981)011<1677:ANORAD>2.0.CO;2.

McDougall, T.J., McIntosh, P.C., 1996. The temporal-residual-mean velocity. Part I: Derivation and the scalar conservation equations. J. Phys. Oceanogr. (ISSN: 0022-3670) 26 (12), 2653–2665. http://dx.doi.org/10.1175/1520-0485(1996)026<2653:TTRMVP>2.0.CO;2.

McDougall, T.J., McIntosh, P.C., 2001. The temporal-residual-mean velocity. Part II: Isopycnal interpretation and the tracer and momentum equations. J. Phys. Oceanogr. (ISSN: 0022-3670) 31 (5), 1222–1246. http://dx.doi.org/10.1175/1520-0485(2001)031<1222:TTRMVP>2.0.CO;2.

Medvedev, A.S., Greatbatch, R.J., 2004. On advection and diffusion in the mesosphere and lower thermosphere: The role of rotational fluxes. J. Geophys. Res.: Atmos. 109 (D7), http://dx.doi.org/10.1029/2003JD003931.

Meneveau, C., Katz, J., 2000. Scale-invariance and turbulence models for large-eddy simulation. Annu. Rev. Fluid Mech. 32 (1), 1–32. http://dx.doi.org/10.1146/annurev.fluid.32.1.1.

Mundt, M.D., Vallis, G.K., Wang, J., 1997. Balanced models and dynamics for the large- and mesoscale circulation. J. Phys. Oceanogr. 27 (6), 1133–1152. http://dx.doi.org/10.1175/1520-0485(1997)027<1133:BMADFT>2.0.CO;2.

Nadiga, B.T., 2008. Orientation of eddy fluxes in geostrophic turbulence. Phil. Trans. R. Soc. A 366 (1875), 2489–2508. http://dx.doi.org/10.1098/rsta.2008.0058.

Pierrehumbert, R.T., 1991. Chaotic mixing of tracer and vorticity by modulated travelling rossby waves. Geophys. Astrophys. Fluid Dyn. 58 (1–4), 285–319. http://dx.doi.org/10.1080/03091929108227343.

Plumb, R., Mahlman, J., 1987. The zonally averaged transport characteristics of the GFDL general circulation/transport model. J. Atmos. Sci. 44, 298–327. http://dx.doi.org/10.1175/1520-0469(1987)044<0298:TZATCO>2.0.CO;2.

Redi, M.H., 1982. Oceanic isopycnal mixing by coordinate rotation. J. Phys. Oceanogr. (ISSN: 0022-3670) 12 (10), 1154–1158. http://dx.doi.org/10.1175/1520-0485(1982)012<1154:OIMBCR>2.0.CO;2.

Shevchenko, I.V., Berloff, P.S., 2015. Multi-layer quasi-geostrophic ocean dynamics in eddy-resolving regimes. Ocean Model. (ISSN: 1463-5003) 94, 1–14. http://dx.doi.org/10.1016/j.ocemod.2015.07.018.

Smith, R.D., Gent, P.R., 2004. Anisotropic Gent–McWilliams parameterization for ocean models. J. Phys. Oceanogr. 34 (11), 2541–2564. http://dx.doi.org/10.1175/JPO2613.1.

Stanley, Z., Bachman, S.D., Grooms, I., 2020. Vertical structure of ocean mesoscale eddies with implications for parameterizations of tracer transport. J. Adv. Modelling Earth Syst. 12 (10), http://dx.doi.org/10.1029/2020MS002151, e2020MS002151.

Sun, L., Haigh, M., Shevchenko, I., Berloff, P., Kamenkovich, I., 2021. On non-uniqueness of the mesoscale eddy diffusivity. J. Fluid Mech. 920, A32. http://dx.doi.org/10.1017/jfm.2021.472.

Treguier, A.M., Held, I.M., Larichev, V.D., 1997. Parameterization of quasigeostrophic eddies in primitive equation ocean models. J. Phys. Oceanogr. 27 (4), 567–580. http://dx.doi.org/10.1175/1520-0485(1997)027<0567:POQEIP>2.0.CO;2.

Visbeck, M., Marshall, J., Haine, T., Spall, M., 1997. Specification of eddy transfer coefficients in coarse-resolution ocean circulation models. J. Phys. Oceanogr. 27 (3), 381–402. http://dx.doi.org/10.1175/1520-0485(1997)027<0381:SOETCI>2.0.CO;2.

Zanna, L., Bolton, T., 2020. Data-driven equation discovery of ocean mesoscale closures. Geophys. Res. Lett. 47 (17), e2020GL088376. http://dx.doi.org/10.1029/2020GL088376, e2020GL088376 10.1029/2020GL088376.

Zurita-Gotor, P., Vallis, G.K., 2009. Equilibration of baroclinic turbulence in primitive equations and quasigeostrophic models. J. Atmos. Sci. 66 (4), 837–863. http://dx.doi.org/10.1175/2008JAS2848.1.